

Structural Investigations of the Nickel-Induced Inhibition of Truncated Constructs of the JMJD2 Family of Histone Demethylases Using X-ray Absorption Spectroscopy

Nitai Charan Giri,[†] Lisa Passantino,[‡] Hong Sun,[‡] Maria Antonietta Zoroddu,[§] Max Costa,[‡] and Michael J. Maroney^{*,†}

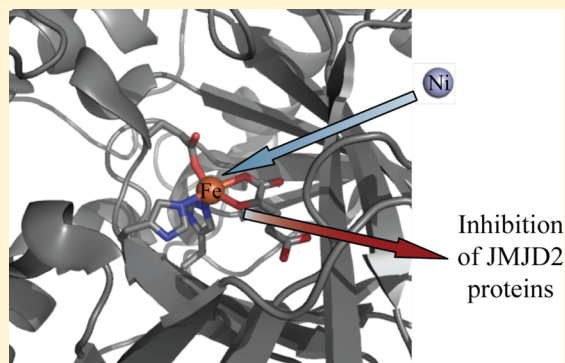
[†]Department of Chemistry, University of Massachusetts, Amherst, Massachusetts 01003, United States

[‡]Department of Environmental Medicine, New York University School of Medicine, New York, New York 10016, United States

[§]Department of Chemistry and Pharmacy, University of Sassari, Sassari, Italy

S Supporting Information

ABSTRACT: Occupational and/or environmental exposure to nickel has been implicated in various types of cancer, and *in vitro* exposure to nickel compounds results in the accumulation of Ni(II) ions in cells. One group of major targets of Ni(II) ions inside the cell consists of Fe(II)- and α KG-dependent dioxygenases. Using JMJD2A and JMJD2C as examples, we show that the JMJD2 family of histone demethylases, which are products of putative oncogenes as well as Fe(II)- and α KG-dependent dioxygenases, are highly sensitive to inhibition by Ni(II) ions. In this work, X-ray absorption spectroscopy (XAS) has been used to investigate the Fe(II) active site of truncated JMJD2A and JMJD2C (1–350 amino acids) in the presence and absence of α KG and/or substrate to obtain mechanistic details of the early steps in catalysis that precede O₂ binding in histone demethylation by the JMJD2 family of histone demethylases. Zinc K-edge XAS has been performed on the resting JMJD2A (with iron in the active site) to confirm the presence of the expected structural zinc site. XAS of the Ni(II)-substituted enzymes has also been performed to investigate the inhibition of these enzymes by Ni(II) ions. Our XAS results indicate that the five-coordinate Fe(II) center in the resting enzyme is retained in the binary and ternary complexes. In contrast, the Ni(II) center is six-coordinate in the resting enzyme and binary and ternary complexes. XAS results indicate that both Fe(II) and Ni(II) bind α KG in the binary and ternary complexes. The electron density buildup that is observed at the Fe(II) center in the presence of α KG and substrate is not observed at the Ni(II) center. Thus, both electronic and steric factors are responsible for Ni-induced inhibition of the JMJD2 family of histone demethylases. Ni-induced inhibition of these enzymes may explain the alteration of the epigenetic mechanism of gene expression that is responsible for Ni-induced carcinogenesis.



Occupational and/or environmental exposure to nickel has been implicated in various types of cancer.^{1–6} However, the precise mechanisms of nickel-induced carcinogenesis are not fully understood.^{7,8} Alterations of epigenetic mechanisms have been proposed to play an important role in nickel-induced carcinogenesis.^{9–11} *In vitro* exposure to nickel compounds results in the accumulation of Ni(II) ions in cells, and recent studies have shown that Fe(II)- and α KG-dependent dioxygenases make up one group of major targets of Ni(II) ions inside the cell.¹² Further, increases in cellular nickel concentration correlate with increases in the global levels of mono- and dimethylated histone H3 Lys9 (H3K9Me1 and H3K9Me2), not by affecting histone methyltransferases but by inhibiting a group of Fe(II)- and α KG-dependent histone demethylases.¹³ It is known that Ni(II) ions inhibit both ABH2 (a DNA demethylase) and JMJD1A (a histone demethylase that demethylates H3K9Me2 and H3K9Me1).¹⁴ It is possible that nickel causes alterations in epigenetic gene expression by

inhibiting the JMJD2 family of histone demethylases, which are among the known Fe(II)- and α KG-dependent enzymes.^{12,15}

Members of the JMJD2 family of histone demethylases (also known as KDM4, lysine specific demethylase 4 histone demethylases) catalyze the demethylation of di- and trimethylated H3K9 and H3K36 (Figure 1).¹⁶ JMJD2 proteins are candidate oncogenes, which contribute to tumor formation.^{17,18} JMJD2A plays an important role in cell proliferation and oncogenesis.¹⁹ JMJD2C has been found to play some role in prostate and breast cancer progression and has been implicated in the regulation of androgen receptor responsive genes.²⁰ Inhibition of JMJD2A and JMJD2C is also known to affect cellular growth.²¹ However, there are limited data available on the enzymology of histone demethylases.

Received: March 4, 2013

Revised: May 14, 2013

Published: May 21, 2013



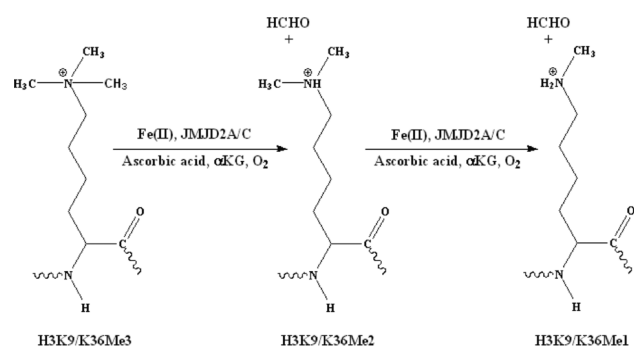


Figure 1. Demethylation of methylated histone tails by JMJD2 proteins.

In this work, XAS has been used to investigate the Fe(II) active site structure of truncated forms of both JMJD2A and JMJD2C (1–350 amino acids) in the presence and absence of α KG and/or substrate to obtain mechanistic details of the early steps (prior to O_2 binding) of histone demethylation by the JMJD2 family of histone demethylases. Full-length JMJD enzymes have high molecular masses (e.g., 150 kDa) and cannot be expressed in large quantities in bacteria but must be expressed in baculovirus and insect cells. The truncated forms of these enzymes, where large quantities of enzyme can be produced in bacteria, were therefore investigated. In addition, XAS has been performed on the Ni(II)-substituted enzymes to understand the nickel-induced inhibition of these enzymes. Crystal structures available for JMJD2 proteins suggest that

these proteins have a zinc binding site involving three Cys ligands and one His ligand, along with the Fe(II) site consisting of a facial triad of protein ligands (2-His-1-carboxylate) and water molecules.^{22–27} Zinc K-edge XAS has been performed on the resting JMJD2A (with iron in the active site) to confirm the presence of the expected structural zinc site. It should be noted that some of these crystal structures feature Ni(II) in place of Fe(II) and also may substitute 2-hydroxyglutarate and *N*-oxalylglycine (N-OG) for α KG (Table 1). These are not competent enzymes and therefore not directly relevant to the Fe(II)- and α KG-dependent demethylation reaction conducted by these enzymes. This study examines the structure of the competent forms of the enzymes in solution and provides a comparison with two related enzymes, the available crystal structures, and with the Ni(II)-inhibited enzymes.

EXPERIMENTAL PROCEDURES

Expression and Purification of Truncated Histone Demethylases. pGEX-4T-1-GST-JMJD2A and pET28a-His₆-JMJD2C constructs were kindly provided by Y. Shi. Protein expression, purification, subsequent cleavage of the GST or His₆ tag, and characterization of the protein products have been reported previously by the Shi lab.^{16,22} *Escherichia coli* BL21(DE3)pLysS competent cells (Novagen) were transformed with pGEX-4T-1-GST-JMJD2A and pET28a-His₆-JMJD2C and were plated and grown overnight at 37 °C on LB medium containing 34 μ g/mL chloramphenicol and 100 μ g/mL ampicillin (for JMJD2A) or 30 μ g/mL kanamycin (for JMJD2C). Single colonies were grown overnight in 150 mL

Table 1. Crystallographically Determined Active Site Structures of the JMJD2 Family of Histone Demethylases

PDB entry	protein	metal ions	cofactor	substrate	ref
3RVH	JMJD2A	Ni/Zn	8-hydroxy-3-(piperazin-1-yl)quinoline-5-carboxylic acid	none	^a
2Q8E	JMJD2A	Ni/Zn	N-OG	none	24
2P5B	JMJD2A	Fe/Zn	N-OG	H3K36Me3 peptide	23
2PXJ	JMJD2A	Fe/Zn	N-OG	H3K36Me1 peptide	23
2Q8C	JMJD2A	Ni/Zn	α KG	H3K9Me3 peptide	24
2OQ6	JMJD2A	Ni/Zn	N-OG	H3K9Me3 peptide	25
2OQ7	JMJD2A	Ni/Zn	N-OG	none	25
2OS2	JMJD2A	Ni/Zn	N-OG	H3K36Me3 peptide	25
2OT7	JMJD2A	Ni/Zn	N-OG	H3K9Me1 peptide	25
2OX0	JMJD2A	Ni/Zn	N-OG	H3K9Me2 peptide	25
2VD7	JMJD2A	Ni/Zn	pyridine-2,4-dicarboxylic acid	none	^a
4A19	JMJD2A	Ni/Zn	Daminozide	none	28
2Q8D	JMJD2A	Ni/Zn	succinic acid	H3K36Me2 peptide	24
2YBK	JMJD2A	Ni/Zn	(2R)-2-hydroxypentanedioic acid	none	26
2WWJ	JMJD2A	Ni/Zn	O-benzyl-N-(carboxycarbonyl)-D-tyrosine	none	29
4GD4	JMJD2A	Ni/Zn	2-(1H-pyrazol-3-yl)pyridine-4-carboxylic acid	none	^a
3PDQ	JMJD2A	Ni/Zn	4'-[(2-aminoethyl)carbamoyl]-2,2'-bipyridine-4-carboxylic acid	none	30
2GP3	JMJD2A	Fe/Zn	none	none	22
2YBP	JMJD2A	Ni/Zn	(2R)-2-hydroxypentanedioic acid	H3K36Me3 peptide	26
2YBS	JMJD2A	Ni/Zn	(2S)-2-hydroxypentanedioic acid	H3K36Me3 peptide	26
3NJY	JMJD2A	Ni/Zn	5-carboxy-8-hydroxyquinoline	none	31
2GP5	JMJD2A	Fe/Zn	α KG	none	22
3U4S	JMJD2A	Ni/Zn	N-(carboxycarbonyl)-D-cysteine	H3K9Me3 peptide	32
2XML	JMJD2C	Ni/Zn	N-OG	none	^a
3DXU	JMJD2D	Fe/Zn	N-OG	none	^a
4HOO	JMJD2D	Ni/Zn	none	none	27
3DXT	JMJD2D	Zn	none	none	^a
4HON	JMJD2D	Ni/Zn	α KG	H3K9Me3 peptide	27

^aThese crystal structures have not been published but are available in the PDB.

cultures containing the antibiotics mentioned above and then diluted to 1:100 in 2 L of fresh LB medium. The cells were grown at 37 °C to an optical density of 0.8 at 600 nm and then induced with isopropyl β -D-1-thiogalactopyranoside (final concentration of 0.2 mM). The cells were grown for an additional 18 h at 18 °C, harvested by centrifugation, resuspended in lysis buffer [50 mM HEPES, 300 mM NaCl, 20 mM imidazole, 0.5 mM TCEP, and 5% glycerol (pH 7.5)], and stored at –80 °C. Upon thawing, the cells were lysed in the presence of PMSF and DNase and then centrifuged to collect the lysate.

Purification of JMJD2A. The supernatant was added to the MagneGST particles in a centrifuge tube (50 mL) and gently agitated for 1 h using a shaker (Orbitron rotator II). Glutathione immobilized on MagneGST particles binds the GST fusion protein. These particles were sequestered by a magnetic field; the liquid phase was removed, and unbound proteins were washed away using wash buffer [50 mM HEPES, 300 mM NaCl, 0.5 mM TCEP, and 5% glycerol (pH 7.5)]. Pure JMJD2A was released from the particles using the wash buffer containing 20 mM glutathione. The purity of JMJD2A was confirmed by a single band with a molecular mass of ~67 kDa on an sodium dodecyl sulfate–polyacrylamide gel electrophoresis (SDS–PAGE) gel (see the Supporting Information). Finally, the GST tag was cleaved from purified protein using a Thrombin CleanCleave Kit (Sigma). Pure JMJD2A (yield of ~1.4 mg/L of cell culture) was separated from uncleaved JMJD2A and the GST tag using a gel filtration column (23.5 mL, Superdex 75 10/300 GL, GE Healthcare Life Sciences) and buffer containing 10 mM HEPES, 300 mM NaCl, 0.5 mM TCEP, and 5% glycerol (pH 7.5). The cleavage of the GST tag was confirmed by SDS–PAGE (see the Supporting Information). This cleavage leaves two extra amino acid residues (GS) on the N-terminus of JMJD2A.^{16,22}

Purification of JMJD2C. The supernatant was loaded onto a Ni-NTA column (27 mL, Kontes FlexColumn, Kimble Chase Kontes) and gently mixed for 1 h using a shaker (Orbitron rotator II). The column was washed with lysis buffer containing 40 mM imidazole. JMJD2C was eluted using lysis buffer with 300 mM imidazole. JMJD2C obtained from the Ni-NTA column was buffer exchanged into a buffer containing 10 mM HEPES, 300 mM NaCl, 0.5 mM TCEP, and 5% glycerol (pH 7.5) and then loaded onto a gel filtration column (23.5 mL, Superdex 200 10/300 GL, GE Healthcare Life Sciences) that was previously equilibrated with the same buffer. JMJD2C was eluted using 2 column volumes (~47 mL) of this buffer. The purity of JMJD2C obtained was confirmed by a single band with a molecular mass of ~44 kDa on an SDS–PAGE gel (see the Supporting Information). The His₆ tag was subsequently cleaved from purified protein using a Thrombin CleanCleave Kit (Sigma) and removed by dialysis against a buffer containing 50 mM HEPES, 300 mM NaCl, 0.5 mM TCEP, and 5% glycerol (pH 7.5) (yield of ~1.1 mg/L of cell culture). The cleavage of the His₆ tag was confirmed by SDS–PAGE (see the Supporting Information). This cleavage will leave 17 extra amino acid residues (GSHMASMTGGQMQMGRGS) on the N-terminus of JMJD2C.^{16,22}

Activity Assay of JMJD2 Proteins. The demethylase activity of JMJD2A and JMJD2C was confirmed using an assay described previously,¹⁴ employing 5 μ g of histone protein (Sigma) in 25 μ L (for JMJD2A) or 30 μ L (for JMJD2C) of reaction buffer containing 50 μ M HEPES (pH 7.8), 100 μ M FeSO₄, 100 μ M ZnSO₄, 1 mM α KG, and 2 mM ascorbic acid.

The demethylase activity assay of JMJD2A and JMJD2C (see the Supporting Information) was used to determine the amount of enzyme used for the nickel inhibition studies. To show the inhibition of JMJD2A and JMJD2C by Ni(II) ions, varying concentrations of NiCl₂ were added to the reaction buffer prior to the addition of JMJD2 proteins. The reaction mixture was incubated at 37 °C for 1 h. We terminated the reaction by adding 6 \times SDS loading dye to a final concentration of 1 \times and heating the mixture at 100 °C for 5 min. The remaining amounts of modified H3K9Me3 in histones were determined by immunoblotting as previously described (Figure 2).¹⁴ The IC₅₀ value for the inhibition of JMJD2C by Ni(II)

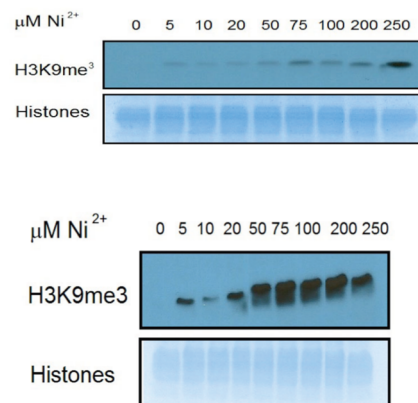


Figure 2. Demethylase activity assay of JMJD2A (top) and JMJD2C (bottom) in the presence of varying concentrations of Ni(II) ions determined by immunoblotting. The lack of any band in the absence of Ni(II) ions indicates the demethylation of all the H3K9Me3. The appearance of bands in the presence of Ni(II) ions indicates that H3K9Me3 remains present because of the inhibition of the enzymes.

was determined from densitometry performed in the gel image using GraphPad Prism 6 (version 6.0a, July 18, 2012) and a sigmoidal dose–response function (see the Supporting Information).

XAS Sample Preparation. Apoprotein was prepared by adding a 5-fold excess of EDTA to the protein solution and incubating it at 4 °C overnight. EDTA was then removed by dialysis against a buffer solution containing 50 mM HEPES, 300 mM NaCl, 2 mM ascorbic acid, and 5% glycerol (pH 7.5). The protein concentration was determined by the Bradford assay using BSA as a standard.³³ Metalated samples were prepared in a Coy chamber and frozen under an N₂ atmosphere. Both JMJD2A and JMJD2C were first metalated with zinc [both of these proteins have a zinc binding site along with the Fe(II) active site] by adding ZnSO₄ (10 mM, 1.25 equiv) to the corresponding apoprotein (~45 μ M). We then removed unbound and nonspecifically bound zinc by adding Chelex 100 beads to the sample, incubating the sample for 20 min, and then decanting the solution via pipet. This zinc-containing protein solution was divided into two portions; one portion was further metalated with iron, and the other portion was metalated with nickel as described below. Fe(JMJD2A/JMJD2C) was prepared by adding a solution of (NH₄)₂Fe(SO₄)₂ (10 mM, 1.25 equiv) in the buffer mentioned above to the zinc-containing protein and incubating the sample for 6 h. We then removed unbound and nonspecifically bound metal by adding Chelex 100 beads to the sample, incubating the sample for 20 min, and then decanting the solution via pipet. The iron

and zinc content of the metalated proteins was determined by ICP-OES using emission at 238.208 and 206.2 nm, respectively. On the basis of a Bradford assay of protein concentration and the metal content found, the metalated JMJD2A and JMJD2C have Fe:Zn:protein ratios of 0.85:0.92:1 and 0.91:0.96:1, respectively.

The same procedure, only substituting NiCl_2 (10 mM, 1.25 equiv) for $(\text{NH}_4)_2\text{Fe}(\text{SO}_4)_2$, was used to prepare Ni(JMJD2A/JMJD2C) complexes. Analysis of the protein concentration and metal content using the same procedure as for the Fe(II) enzyme (the nickel concentration was measured using the 231.604 nm emission) gave Ni:Zn:protein ratios of 0.90:0.94:1 for JMJD2A and 0.94:0.96:1 for JMJD2C.

From the Fe(JMJD2A/JMJD2C) preparation described above, a total of three samples of each protein were prepared for XAS experiments. The first sample contained only the metalated protein, hereafter termed Fe(JMJD2A/JMJD2C). The second sample contained Fe(JMJD2A/JMJD2C) and 1.0 equiv of αKG , hereafter termed Fe(JMJD2A/JMJD2C)- αKG . Finally, the third sample contained Fe(JMJD2A/JMJD2C), 1.0 equiv of αKG , and 2 equiv of histone from calf thymus (Sigma), hereafter termed Fe(JMJD2A/JMJD2C)- αKG + substrate. The iron contents were 0.64 mM (for 0.75 mM JMJD2A protein) and 0.62 mM (for 0.68 mM JMJD2C protein) for the Fe(JMJD2A) and Fe(JMJD2C) samples, respectively; 0.63 mM (for 0.74 mM JMJD2A protein) and 0.61 mM (for 0.67 mM JMJD2C protein) for the Fe(JMJD2A)- αKG and Fe(JMJD2C)- αKG samples, respectively; and 0.61 mM (for 0.72 mM JMJD2A protein) and 0.59 mM (for 0.65 mM JMJD2C protein) for the Fe(JMJD2A)- αKG + substrate and Fe(JMJD2C)- αKG + substrate samples, respectively, as determined by ICP-OES. Three analogous samples were prepared from Ni(JMJD2A/JMJD2C). The nickel contents were ~0.60 mM (for 0.67 mM JMJD2A protein) and 0.63 mM (for 0.67 mM JMJD2C protein) for the Ni(JMJD2A) and Ni(JMJD2C) samples, respectively; 0.59 mM (for 0.66 mM JMJD2A protein) and 0.62 mM (for 0.66 mM JMJD2C protein) for the Ni(JMJD2A)- αKG and Ni(JMJD2C)- αKG samples, respectively; and 0.57 mM (for 0.63 mM JMJD2A protein) and 0.60 mM (for 0.64 mM JMJD2C protein) for the Ni(JMJD2A)- αKG + substrate and Ni(JMJD2C)- αKG + substrate samples, respectively, as determined by ICP-OES. The protein examined by Zn K-edge XAS had a zinc content of 0.69 mM (for 0.75 mM JMJD2A protein). The samples (60 μL) were added via syringe to polycarbonate sample holders with kapton windows and frozen in liquid N_2 for XAS data collection.

X-ray Absorption Spectroscopy. XAS data collection and analysis were performed as reported previously.^{34,35} Iron, nickel, and zinc K-edge data were collected at 10 K using a liquid He cryostat (Oxford Instruments) on beamline 7-3 at the Stanford Synchrotron Radiation Lightsource (SSRL). Beamline optics consisted of a Si(220) double-crystal monochromator and a single Rh-coated mirror for harmonic rejection. X-ray fluorescence was collected using a 30-element Ge detector (Canberra). Scattering was minimized by placing a set of Soller slits with a (Z-1) element (Mn, Co, or Cu) filter between the sample chamber and the detector. The energy of each metal K-edge was calibrated to the first inflection point of the relevant metal foil (7112.5 eV for iron, 8331.6 eV for nickel, and 9660.7 eV for zinc). Extended X-ray absorption fine structure (EXAFS) data were collected to $k = 14 \text{ \AA}^{-1}$ above the edge energy for all the samples.

XAS data analysis was performed using EXAFS123³⁶ for XANES analysis and SixPack³⁷ for EXAFS analysis. Scattering parameters for SixPack fitting were generated using FEFF 8.³⁸ For the data presented here, 12 scans were averaged for iron-containing samples, eight scans for nickel-containing samples, and six scans for the zinc data. The averaged spectra were background corrected and normalized in SixPack, which uses the AUTOBK routine of IFEFFIT.^{37,39,40} For XANES analysis, the edge energy reported was taken to be the maximum of the first derivative in the edge region. For pre-edge XANES analysis, a Gaussian function was used to fit the baseline of the pre-edge region, with a 75% Gaussian and 25% Lorentzian function used to fit the rise in the fluorescence at the edge. Gaussian peaks were added to the baseline-corrected spectrum to account for any peaks in the pre-edge region. The areas of these peaks were taken as a measure of their intensities. The intensity of the peak associated with a $1s \rightarrow 3d$ electronic transition was then used to indicate the coordination number and/or geometry of the metal sites.^{41–43}

For EXAFS analysis, the averaged spectra were first converted to k space. EXAFS data were fit over a k range of 2–12.5 \AA^{-1} with the exception of Fe(JMJD2A)- αKG and Ni(JMJD2C)- αKG + substrate, where a k range of 2–12 \AA^{-1} was used because of poorer signal:noise ratios at high k values. For the zinc K-edge EXAFS analysis of the resting JMJD2A (with iron in the active site), a k range of 2–13.5 \AA^{-1} was used. The k^3 -weighted data were fit in r space. Structural models of the metal sites involving coordination numbers from 2 to 7 were systematically evaluated for all possible combinations of N/O and S donors by holding the number of scattering atoms in each shell to integer values (see the Supporting Information). The number of histidine imidazole ligands involved in the coordination sphere was estimated by multiple-scattering analyses, as described previously.^{44–46} Amplitudes and phase shifts for multiple-scattering paths for Fe-Im ligands were generated using FEFF 8 with the coordinates of an Fe-Im ligand obtained from the crystal structure of human PHF8 (PDB entry 3K3O). For Ni-Im and Zn-Im ligands, the crystal structures of PHF2 (PDB entry 3PUA) and JMJD2A (PDB entry 2GP3) were used, respectively. Scattering paths of similar lengths were combined in one shell as described by Tierney et al.^{45,46} to decrease the number of variables in each fit. During the fitting process, coordination numbers were constrained to be integer values and a scale factor of 0.9 was used. Bond lengths (r), σ^2 , and a single value of ΔE_0 were allowed to vary in each fit. For αKG and ascorbate ligands, the best models including imidazole ligands were further screened using multiple-scattering analysis employing rigid O–C–C–O five-membered chelate rings with parameters obtained from FEFF 8 and the structures mentioned above. The crystal structure of trimethylreductic acid (an ascorbic acid analogue) was used to generate the parameters for the chelate ring in the resting enzymes.⁴⁷ The crystal structures of PHF2 (PDB entry 3PUA) and PHF8 (PDB entry 3K3O) were used to generate the parameters for the chelate ring in the αKG -containing complexes. In this analysis, the distances in the chelate ring were constrained to vary with a single value of Δr and σ^2 . With the exception of resting enzymes with Fe(II) and Ni(II), the fits were improved by the substitution of two N/O donors in the first coordination sphere by the chelate ring, which adds two carbon atoms to the second coordination sphere in addition to replacing two N/O atoms in the first coordination sphere.

Table 2. XAS Analysis of JMJD2A and JMJD2C Samples

sample	XANES analysis			EXAFS analysis					
	edge E (eV)	1s \rightarrow 3d peak area ($\times 10^{-2}$ eV)	coordination number	shell	r (Å) ^a	σ^2 ($\times 10^{-3}$ Å ²) ^b	ΔE_0 (eV)	reduced χ^2	%R ^c
Fe(JMJD2A)	7123.1(2)	13(1)	5	3 N/O 2 N/O (2Im)	2.00(2) 2.16(2)	2(2) 5(2)	−9(2)	9.27	2.3
Fe(JMJD2A) Zn site	9661.2(2)	NA ^d	NA ^d	1 Im 3 S	2.08(2) 2.34(4)	3(2) 3(3)	−9(1)	13.1	0.9
Fe(JMJD2A)- α KG	7122.5(2)	13(1)	5	3 N/O 2 N/O (2Im) 3 N/O (2Im) 1 O 1 O 1 C 1 C	2.09(2) 1.93(4) 2.05(2) [1.90(3)] ^e [2.11(3)] ^e [2.62(3)] ^e [2.72(3)] ^e	2(2) 4(4) 1(1) 2(2)	−12(4) 0(4)	7.88 4.03	7.6 5.0
Fe(JMJD2A)- α KG + substrate	7121.9(2)	12(1)	5	3 N/O 2 N/O (2Im) 3 N/O (2Im) 1 O 1 O 1 C 1 C	1.98(2) 2.13(3) 2.00(1) [1.96(5)] ^e [2.17(5)] ^e [2.68(5)] ^e [2.78(5)] ^e	2(2) 6(3) 2(1) 4(2)	−8(2) 1(2)	11.4 7.89	4.0 2.2
Ni(JMJD2A)	8344.1(2)	3.7(7)	6	6 N/O (2Im)	2.08(1)	4(1)	5(1)	6.26	2.7
Ni(JMJD2A)- α KG	8344.1(2)	3.6(6)	6	4 N/O 2 N/O (2Im) 4 N/O (2Im) 1 O 1 O 1 C 1 C	2.14(1) 1.98(1) 2.08(2) [2.00(6)] ^e [2.05(6)] ^e [2.67(6)] ^e [2.69(6)] ^e	1(1) 1(1) 3(2) 5(5)	−2(2) 5(3)	5.77 3.55	3.3 3.1
Ni(JMJD2A)- α KG + substrate	8344.1(2)	2.9(8)	6	4 N/O 2 N/O (2Im) 4 N/O (2Im) 1 O 1 O 1 C 1 C	2.14(1) 1.99(1) 2.09(2) [1.98(4)] ^e [2.03(4)] ^e [2.65(4)] ^e [2.67(4)] ^e	1(1) 1(1) 3(1) 4(3)	−1(1) 4(2)	2.74 1.59	3.4 3.0
Fe(JMJD2C)	7122.9(2)	11(1)	5	3 N/O 2 N/O (2Im)	1.99(1) 2.15(1)	1(1) 2(1)	−11(1)	1.37	2.8
Fe(JMJD2C)- α KG	7122.5(2)	12(1)	5	3 N/O 2 N/O (2Im) 3 N/O (2Im) 1 O 1 O 1 C 1 C	2.01(2) 2.17(4) 2.05(2) [1.92(7)] ^e [2.13(7)] ^e [2.64(7)] ^e [2.74(7)] ^e	3(2) 9(7) 4(1) 6(4)	−9(2) −2(4)	2.08 1.28	2.5 1.5
Fe(JMJD2C)- α KG + substrate	7122.1(2)	10(2)	5	3 N/O	2.19(2)	2(1)	−10(2)	32.4	4.3

Table 2. continued

sample	XANES analysis			EXAFS analysis					
	edge E (eV)	1s \rightarrow 3d peak area ($\times 10^{-2}$ eV)	coordination number	shell	r (Å) ^a	σ^2 ($\times 10^{-3}$ Å ²) ^b	ΔE_0 (eV)	reduced χ^2	%R ^c
Ni(JMJD2C)	8344.3(2)	2.9(1)	6	2 N/O (2Im)	2.04(2)	3(2)			
				3 N/O (2Im)	2.16(1)	2(1)	−1(2)	24.7	3.3
				1 O	[2.01(2)] ^e	2(2)			
				1 O	[2.22(2)] ^e				
				1 C	[2.73(2)] ^e				
				1 C	[2.83(2)] ^e				
				6 N/O (2Im)	2.09(1)	5(1)	6(1)	7.88	3.6
				4 N/O (2Im)	2.13(2)	4(4)	−3(2)	10.5	4.6
				2 N/O (2Im)	1.98(4)	3(2)			
				4 N/O (2Im)	2.04(2)	4(3)	8(2)	7.89	3.5
Ni(JMJD2C)-αKG	8344.5(2)	2.8(7)	6	1 O	[2.09(3)] ^e	3(3)			
				1 O	[2.14(3)] ^e				
				1 C	[2.76(3)] ^e				
				1 C	[2.78(3)] ^e				
				6 N/O (2Im)	2.08(1)	3(1)	6(2)	7.78	4.8
				4 N/O (2Im)	2.07(1)	1(1)	3(3)	5.85	2.9
				1 O	[1.96(8)] ^e	10(9)			
				1 O	[2.01(8)] ^e				
				1 C	[2.63(8)] ^e				
				1 C	[2.65(8)] ^e				
Ni(JMJD2C)-αKG + substrate	8344.1(2)	2.7(9)	6	6 N/O (2Im)	2.08(1)	3(1)	6(2)	7.78	4.8
				4 N/O (2Im)	2.07(1)	1(1)	3(3)	5.85	2.9

^a r is the radial distance between the metal and ligand. Distances in brackets correspond to atoms in a O—C—O chelate ring and were constrained to vary with a single value of Δr for the chelate ring. ^b σ^2 is the root-mean-square disorder in the metal–ligand distance. ^c R is the goodness of fit. Numbers in parentheses represent the standard deviation for least-squares fits. ^dNot available. ^eDistances in [] correspond to atoms in O—C—O chelate ring and were constrained to vary with a single value of Δr for the chelate ring.

To compare different fits in the same data set, IFEFFIT uses three goodness of fit parameters χ^2 (eq 1) and reduced χ^2 and R (eq 2):

$$\chi^2 = \frac{N_{\text{idp}}}{N_{\text{e}}^2} \sum_{i=1}^N \{ [\text{Re}[\tilde{\chi}_{\text{data}}(f_i) - \tilde{\chi}_{\text{model}}(f_i)]]^2 + [\text{Im}[\tilde{\chi}_{\text{data}}(f_i) - \tilde{\chi}_{\text{model}}(f_i)]]^2 \} \quad (1)$$

$$R = \left[\sum_{i=1}^N \{ [\text{Re}[\tilde{\chi}_{\text{data}}(f_i) - \tilde{\chi}_{\text{model}}(f_i)]]^2 + [\text{Im}[\tilde{\chi}_{\text{data}}(f_i) - \tilde{\chi}_{\text{model}}(f_i)]]^2 \} \right] / \left[\sum_{i=1}^N \{ [\text{Re}[\tilde{\chi}_{\text{data}}(f_i)]]^2 + [\text{Im}[\tilde{\chi}_{\text{data}}(f_i)]]^2 \} \right] \quad (2)$$

where N_{idp} is the number of independent data points, N_{e}^2 is the number of uncertainties to minimize, Re represents the real part of the EXAFS fitting function, Im represents the imaginary part of the EXAFS fitting function, and $\tilde{\chi}(f_i)$ is the Fourier-transformed data or model function. Reduced $\chi^2 = \chi^2 / (N_{\text{ind}} - N_{\text{varys}})$ (where N_{varys} is the number of refining parameters) and

represents the degrees of freedom in the fit. IFEFFIT also calculates R for the fit, which is given by eq 2 and is scaled to the magnitude of the data, making it proportional to χ^2 . To compare different models (fits), the R factor and reduced χ^2 parameters can be assessed, in which case both parameters should be minimized. Although R will always improve with an increasing number of shells (adjustable parameters), reduced χ^2 will go through a minimum and then increase, indicating that the model is overfitting the data. Best fits were judged by using two goodness of fit parameters, reduced χ^2 and R , and the deviation of σ^2 from typical values.

RESULTS

Activity Assay of JMJD2 Proteins. The demethylase activity of JMJD2A shows that it took 9 μg of enzyme to demethylate all the H3K9Me3. JMJD2C was slightly more active; it took 6 μg of enzyme to demethylate all H3K9Me3 (see the Supporting Information). These amounts of enzymes were subsequently used to show the inhibition of JMJD2A and JMJD2C by Ni(II) ions.

Inhibition of the demethylase activity of JMJD2A and JMJD2C was observed in the presence of a varying concentration of Ni(II) ions (Figure 2). It should be noted that JMJD2C is inhibited at a much lower concentration of Ni(II) ions, 50 μM , than JMJD2A (250 μM). This is due in

part to the fact that a smaller amount of enzyme was used for the JMJD2C assay than for the JMJD2A assay. The Ni(II):JMJD2 molar ratios for the inhibition of JMJD2A and JMJD2C are 28.4 and 10.6, respectively. These molar ratios indicate that JMJD2C is more sensitive to Ni(II) inhibition than is JMJD2A. We were able to calculate IC_{50} value for the inhibition of JMJD2C by Ni(II) ions using densitometry (see the Supporting Information). The IC_{50} value for the inhibition of JMJD2C by Ni(II) ions is 20.5 μ M, which is similar to that previously determined for JMJD1A (25 μ M).¹⁴

X-ray Absorption Spectroscopy. XANES Analysis. The analysis of XANES data provides information about the coordination number and geometry of the metal site^{41–43} and is summarized for the JMJD2A and JMJD2C proteins in Table 2 and Figures 3–5. Both Fe(II) and Ni(II) give rise to peaks

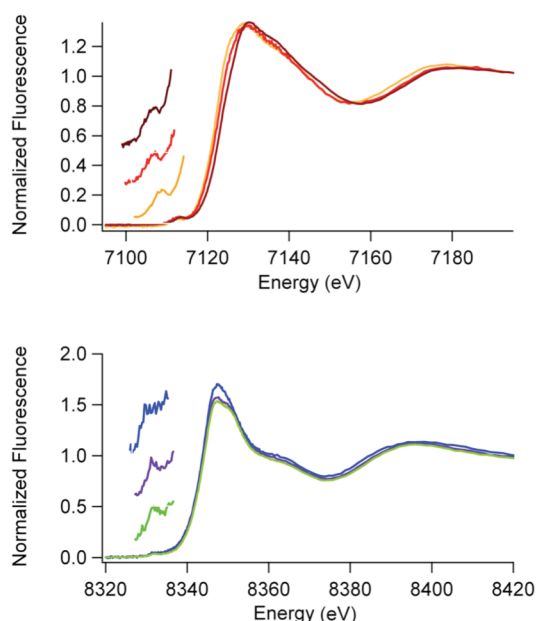


Figure 3. Fe K-edge XANES spectra (top) of Fe(JMJD2A) (brown), Fe(JMJD2A)- α KG (red), and Fe(JMJD2A)- α KG + substrate (orange). Ni K-edge XANES spectra (bottom) of Ni(JMJD2A) (blue), Ni(JMJD2A)- α KG (purple), and Ni(JMJD2A)- α KG + substrate (green). Insets show the expansions of the pre-edge XANES region showing peaks associated with 1s \rightarrow 3d transitions.

associated with 1s \rightarrow 3d electronic transitions (at \sim 7113 and \sim 8332 eV, respectively) that are observed in the pre-edge region of the K-edge XANES spectra in all the histone demethylase samples. The intensities (peak areas) of these peaks depend on the coordination number and geometry of the metal sites.^{41–43} Comparison of the peak areas measured for the histone demethylase samples with those obtained for coordination compounds with known coordination numbers and/or geometries provides a measure of coordination number and geometry for the enzyme metal sites. The peak areas obtained for all of the iron-containing histone demethylase samples ($10\text{--}13 \times 10^{-2}$ eV) are indicative of five-coordinate sites (typical values are $8\text{--}13 \times 10^{-2}$ eV).^{42,43} This is in agreement with the crystal structure of JMJD2A obtained in the presence or absence of α KG.²²

XANES data (Table 2 and Figures 3 and 4) for the iron-containing samples show a decrease in iron K-edge energy from Fe(JMJD2A/JMJD2C) to Fe(JMJD2A/JMJD2C)- α KG to Fe-(JMJD2A/JMJD2C)- α KG + substrate. This indicates an

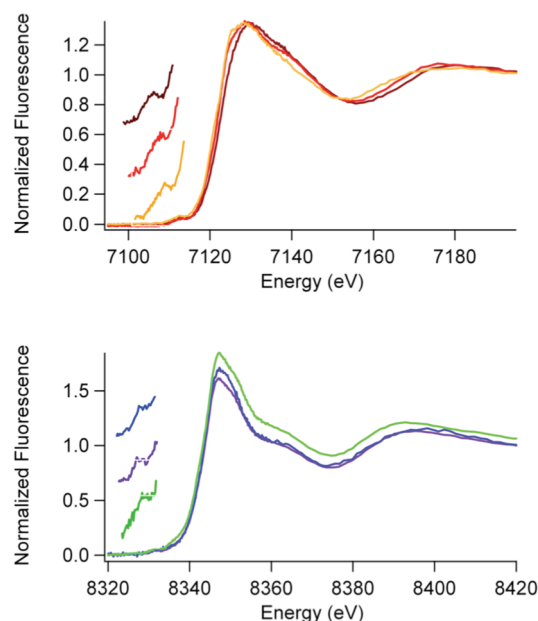


Figure 4. Fe K-edge XANES spectra (top) of Fe(JMJD2C) (brown), Fe(JMJD2C)- α KG (red), and Fe(JMJD2C)- α KG + substrate (orange). Ni K-edge XANES spectra (bottom) of Ni(JMJD2C) (blue), Ni(JMJD2C)- α KG (purple), and Ni(JMJD2C)- α KG + substrate (green). Insets show the expansions of the pre-edge XANES region showing peaks associated with 1s \rightarrow 3d transitions.

increase in the electron density at the iron center that will eventually bind O₂ in the presence of both the α KG cofactor and the substrate. No changes in the coordination number of the iron site are observed in any of the iron-containing samples. In contrast, XANES data (Table 2 and Figures 3 and 4) for nickel-containing JMJD2A and JMJD2C samples do not show any systematic decrease in the edge energy in the presence of α KG and/or the substrate, indicating that very little change in the electron density occurs at the nickel site in the presence of α KG and/or the substrate. Unlike the analogous iron-containing samples, the 1s \rightarrow 3d peak areas ($2.7\text{--}3.7 \times 10^{-2}$ eV) are indicative of six-coordinate nickel sites (typical values of $0.6\text{--}4 \times 10^{-2}$ eV)⁴¹ in all the nickel-containing samples. This result is in agreement with the crystal structures of nickel-containing JMJD2A obtained in the presence of α KG and substrate^{24,25} and suggests that the electronic interaction of Ni(II) with α KG is quite different from that of Fe(II). The result is also in agreement with the crystal structure of JMJD2C in a complex with Ni(II) and N-OG.

Zn(II) does not give rise to peaks associated with 1s \rightarrow 3d electronic transitions in the pre-edge XANES region of the K-edge spectra. However, the shape and intensity of the absorption edge can be used to obtain the structural information about the zinc site in resting JMJD2A [with iron in the active site (Figure 5)]. The intensity of the zinc K-edge XANES spectrum of the resting enzyme indicates the presence of a four-coordinate zinc site.⁴⁸ The presence of two XANES peaks at 9664 and 9669 eV indicates the presence of a zinc site with a mixed environment of N/O and S ligands.⁴⁸

EXAFS Analysis. EXAFS analysis provides information regarding the number (N) and the type of ligands bound to a metal and metric details of the metal site structure. The information obtained from the best fits of the data is summarized in Table 2 and Figures 5–7. For all the histone demethylase samples, the determined N values are in

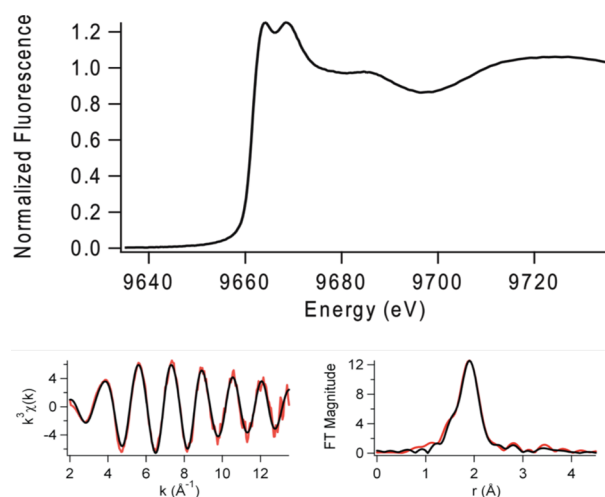


Figure 5. Zn K-edge XAS of resting JMJD2A (with iron in the active site): XANES spectrum (top) and EXAFS analysis [bottom; left, unfiltered, k^3 -weighted EXAFS spectra in red and fit in black (from Table 2); right, Fourier-transformed EXAFS data and fit].

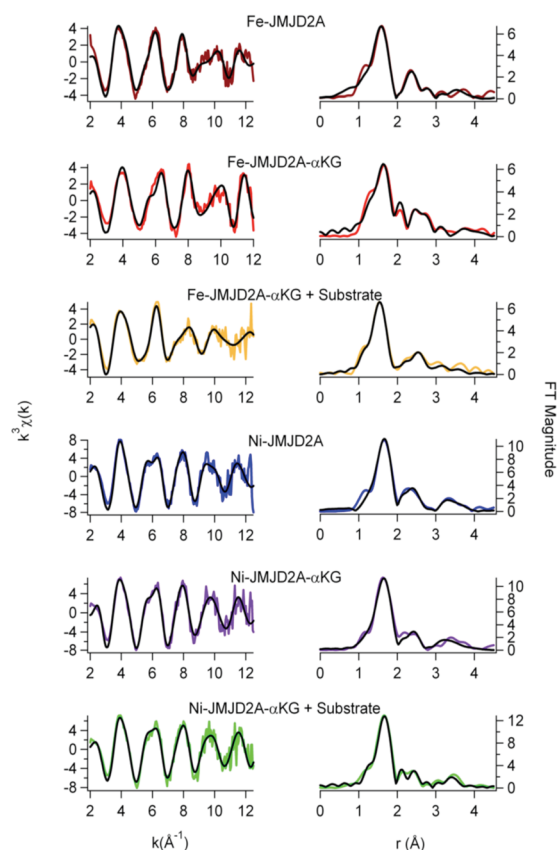


Figure 6. EXAFS analysis of JMJD2A. The left panels show unfiltered, k^3 -weighted EXAFS spectra (colored lines) and fits [black lines (from Table 2)]. The right panels show Fourier-transformed EXAFS data and fits.

agreement with the XANES analysis (*vide supra*). The best fit for both Fe(JMJD2A) and Fe(JMJD2C) EXAFS data consists of five N/O donors, of which two are imidazole ligands. The three remaining ligands are consistent with coordination by the active site Glu ligand and two aqua ligands, consistent with the crystal structure of the catalytic domain of JMJD2A.²² Multiple-scattering analyses that include a five-membered O—C—C—O

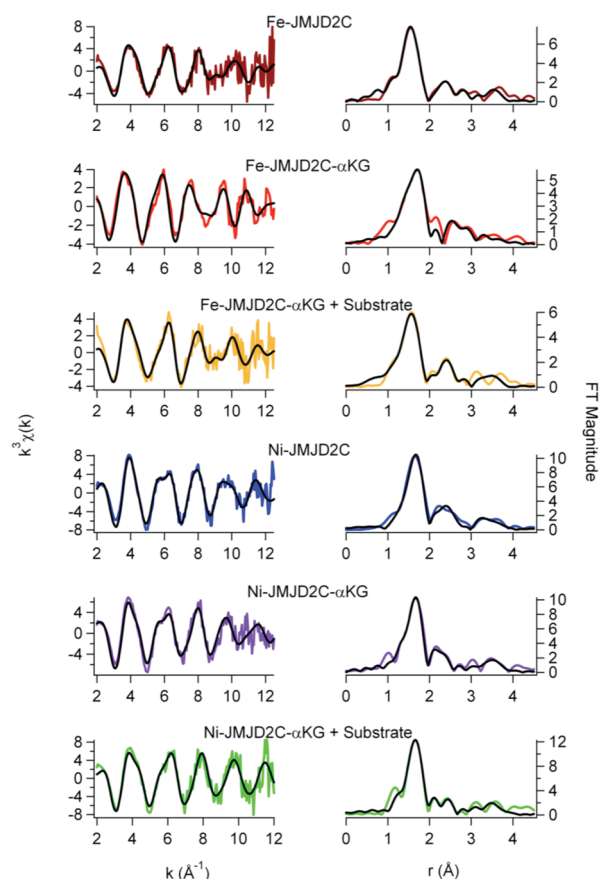


Figure 7. EXAFS analysis of JMJD2C. The left panels show unfiltered, k^3 -weighted EXAFS spectra (colored lines) and fits [black lines (from Table 2)]. The right panels show Fourier-transformed EXAFS data and fits.

chelate ring do not support binding of ascorbate to the iron center in any of the resting enzymes, as was seen for ABH2³⁵ and 1-aminocyclopropane-1-carboxylate oxidase (ACCO).^{49,50} Upon reconstitution with Ni(II), the best fit for both JMJD2A and JMJD2C features six N/O donors, two of which are His imidazole ligands. Multiple-scattering analyses involving O—C—C—O chelate rings do not show ascorbate binding to the nickel center in either JMJD2A or JMJD2C. Thus, the four remaining ligands are consistent with the expected coordination of the active site Glu ligand and the three aqua ligands.

The zinc K-edge EXAFS analysis of resting JMJD2A (with iron in the active site) is shown in Table 2 and Figure 5. In agreement with expectations based on the XANES analysis (*vide supra*) and the amino acid sequence, the best fit for zinc K-edge EXAFS data of the resting JMJD2A consists of a four-coordinate tetrahedral zinc site with the ligation from one N/O donor ligand (from imidazole) at 2.08 Å and three S donor ligands (from cysteine) at 2.34 Å. The observed Zn—S distances are typical of tetrahedral zinc sites (2.33 Å).⁵¹ The FT XAS spectrum for the resting JMJD2A shows outer peaks at 2.8, 3.4, and 3.8 Å. These are similar to the peaks observed for a Zn(Cys)₃His peptide complex⁵¹ and are consistent with expectations from amino acid sequence homologies, which feature a C(X)₅H(X)₆CXC motif, and consistent with the crystal structure of the catalytic domain of JMJD2A²² and JMJD2D.²⁷

Addition of αKG to either Fe(JMJD2A) or Fe(JMJD2C) does not cause any net change in the number of ligands in the

first coordination sphere, as it still contains five N/O donors, including two imidazole ligands (Table 2 and Figures 6 and 7). This is in agreement with the crystal structure of Fe(JMJD2A) in the presence of α KG.²² However, changes in the second coordination sphere are apparent (Figures 6 and 7). Multiple-scattering analyses involving O–C–C–O five-membered chelate rings were performed to assess α KG binding. These fits use a single distance parameter and a single value of σ^2 for all the atoms in the chelate ring. Therefore, these fits do not contain more adjustable parameters than the corresponding fit without the chelate ring and are thus directly comparable. The results show that in contrast to the data for resting enzymes, both R and χ^2 are improved by the replacement of two first coordination shell N/O donors by one O–C–C–O unit (Table 2). Using the chelate model, two second-coordination sphere carbon atoms at 2.62 and 2.72 Å for JMJD2A and 2.64 and 2.74 Å for JMJD2C are found. The presence of two second-coordination sphere carbon atoms is consistent with bidentate α KG binding to the iron center. While it is true that the EXAFS arising from second-sphere carbon atoms is sometimes suppressed by destructive interference from other scattering atoms,^{52–54} this is not the case for the samples studied here. In this case, the amplitude ratio for the α KG second-sphere carbon atoms calculated by FEFF 8 (~45, considering M–O to be ~100) is comparable to that of second-sphere carbon atoms in imidazole (~40, considering M–N to be 100). This is consistent with the observation of second-sphere carbon atoms using EXAFS in other samples.^{52–56} The decrease in the iron K-edge energy in the presence of α KG further supports the binding of α KG to the metal center. [It is important to note that the model obtained from the PHF8 crystal structure features two metal–carbon distances that are below the resolution of the EXAFS data (Table 2 and Figures 6 and 7).] The similar metal–carbon distances, coupled with the errors [2.62(3) and 2.72(3) Å for JMJD2A and 2.64(7) and 2.74(7) Å for JMJD2C], indicate that the difference in the distances to the carbon atoms is not resolved in the EXAFS of JMJD2A or JMJD2C.

Addition of α KG to either Ni(JMJD2A) or Ni(JMJD2C) does not change the first coordination sphere, as the nickel site still consists of six N/O donors, two of which are imidazole ligands. This is consistent with the crystal structure of Ni(JMJD2A) with N-OG²⁴ and Ni(JMJD2C) with N-OG, which shows the presence of a six-coordinate nickel site. Using the chelate model outlined above, two second-sphere carbon atoms at 2.67 and 2.69 Å for Ni(JMJD2A)- α KG and 2.76 and 2.78 Å for Ni(JMJD2C)- α KG are observed. The presence of the second-coordination sphere carbon atoms indicates the bidentate binding of α KG to the nickel center.

Addition of substrate to the α KG complexes of the iron- and nickel-containing histone demethylases does not change the structure of the metal sites significantly (Table 2 and Figures 6 and 7). The iron site remains five-coordinate with five N/O donor ligands, two of which are imidazoles. The O–C–C–O five-membered chelate rings observed for the α KG complexes are retained in the presence of the substrate. Using the chelate model for α KG binding, two second-sphere carbon atoms at 2.68 and 2.78 Å for Fe(JMJD2A) and 2.73 and 2.83 Å for Fe(JMJD2C) are observed. The presence of the second-sphere carbon atoms confirms that bidentate binding of α KG to the iron center is retained in the presence of the substrate. The nickel site remains six-coordinate with six N/O donor ligands, two of which are imidazoles. This is in agreement with the

crystal structure of JMJD2A in the ternary complex formed with a histone H3K9Me3 peptide and α KG.²⁵ The O–C–C–O five-membered chelate rings are also retained in the nickel-containing samples in the presence of the substrate. Using the chelate ring model, two second-sphere carbon atoms at 2.65 and 2.67 Å for Ni(JMJD2A) and 2.63 and 2.65 Å for Ni(JMJD2C) are observed. The presence of the second-coordination sphere carbon atoms indicates the bidentate binding of α KG to the nickel center is retained in the presence of the substrate.

DISCUSSION

Histone tails undergo a number of posttranslational modifications, including acetylation, methylation, phosphorylation, and ubiquitination.⁵⁷ Histone methylation occurs on both lysine and arginine residues. Several lysine residues of histones H3 and H4 (H3K4, H3K9, H3K27, H3K36, H3K79, and H4K20) undergo methylation.^{58,59} Histone methylation can contribute to several biological processes, including heterochromatin formation, X-inactivation, genome imprinting, and silencing of homeotic genes.^{60–62} Histone methylation was considered as a permanent modification for many years.^{63,64} However, the identification of the H3K4 specific lysine demethylase (LSD1) suggested that histone methylation is reversible.⁶⁵ Histone demethylase JHDM1 (Jumonji domain containing histone demethylase 1), which specifically demethylates H3K36Me2, also indicated that histone methylation is reversible.⁶⁶ Both LSD1 and JHDM1 demethylate only mono- and dimethylated histones.^{65,66} The inability of LSD1 and JHDM1 to demethylate trimethylated histone Lys residues raised the possibility of unknown histone demethylases that can demethylate trimethylated histones.

The JMJD2 family of histone demethylases consists of six members, the long group (JMJD2A, JMJD2B, and JMJD2C) and the short group (JMJD2D, JMJD2E, and JMJD2F).⁶⁷ Short group enzymes contain only JmjN and JmjC domains, whereas the long group enzymes contain two PHD domains and two Tudor domains in addition to the JmjN and JmjC domains.¹⁶ JMJD2A–C catalyze demethylation of di- and trimethylated forms of H3K9 and di- and trimethylated forms of H3K36 residues (Figure 1), but not mono-, di-, or trimethylated H3K4, H3K27, and H4K20 sites, while JMJD2D and JMJD2E demethylate di- and trimethylated forms of only H3K9.⁶⁸ Sequence alignment of the JMJD2 family members shows a high degree of similarity (55.7% identical and 81.71% similar) within the first 350 amino acids.²² JMJD2A and JMJD2C are the most studied members of this family.⁶⁸ Studies of some of the truncated enzymes showed that they catalyze the demethylation reactions with the same site specificity as the full-length enzyme.¹⁶ Truncated enzymes were used in this study because of difficulties in the heterologous expression of the full-length enzymes in *E. coli*. Using JMJD2A and JMJD2C as examples, we show that the JMJD2 family of histone demethylases is sensitive to inhibition by Ni(II) ions (Figure 2).

A healthy unexposed adult has ~7.3 μ g of Ni/kg of body weight.⁶⁹ The unexposed population in the United States has 2.6 μ g/L (0.0443 μ M) nickel in blood serum.⁷⁰ Endocytosis of a 1.5 or 4.0 μ m crystalline NiS particle can result in an intracellular Ni(II) concentration of 0.25 or 4.75 M, respectively.⁶⁹ Results obtained in this work indicate that JMJD2 proteins will not be inhibited by normal nickel exposures but would be inhibited by nickel concentrations

Table 3. Results Obtained from XAS Analysis of JMJD2A and JMJD2C Samples

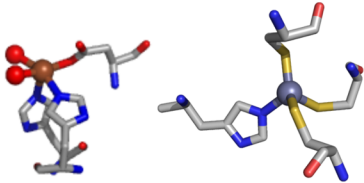
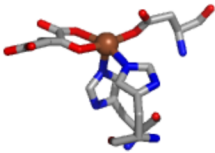
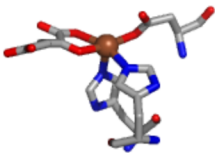
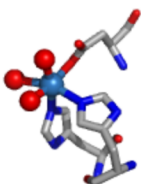

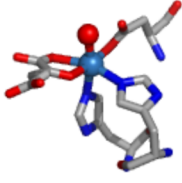
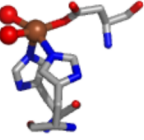
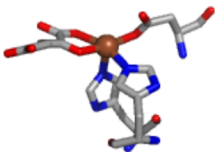
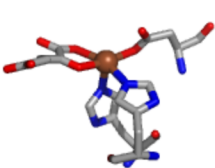
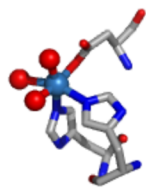
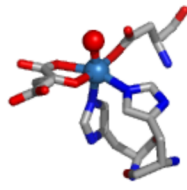
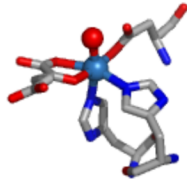
Protein	Metal ion	Cofactor	Substrate	Active site
JMJD2A	Fe/Zn	No	No	
JMJD2A	Fe/Zn	αKG	No	
JMJD2A	Fe/Zn	αKG	Yes	
JMJD2A	Ni/Zn	No	No	
JMJD2A	Ni/Zn	αKG	No	
JMJD2A	Ni/Zn	αKG	Yes	
JMJD2C	Fe/Zn	No	No	
JMJD2C	Fe/Zn	αKG	No	
JMJD2C	Fe/Zn	αKG	Yes	

Table 3. continued

Protein	Metal ion	Cofactor	Substrate	Active site
JMJD2C	Ni/Zn	No	No	
JMJD2C	Ni/Zn	α KG	No	
JMJD2C	Ni/Zn	α KG	Yes	

resulting from endocytosis of particulate nickel compounds. Inhibition of histone demethylases by Ni(II) ions changes global as well as gene specific levels of histone methylation.¹³ This would lead to alteration of gene expression via epigenetic mechanisms, which have been previously implicated in nickel-induced carcinogenesis. In this work, XAS was performed to examine the structures of Fe(II)– and Ni(II)–JMJD2A and –JMJD2C complexes to obtain mechanistic details of histone demethylation by the JMJD2 family of enzymes and their inhibition by Ni(II) ions.

Structures of the Early Intermediates in the JMJD2A and JMJD2C Reaction Cycles by XAS. The structural information obtained from XAS analysis (Table 3) is in general agreement with the expectations from the available crystal structures of the catalytic core domain of JMJD2 proteins (Table 1). Resting Fe(JMJD2A) and Fe(JMJD2C) show the presence of a five-coordinate iron site involving two imidazole ligands and three other N/O donor ligands (Table 3), which are likely Glu (residue 190 for JMJD2A and residue 192 for JMJD2C) and two water molecules observed in the crystal structures of JMJD2A.²² The two very long Fe–O distances involving two aqua ligands at 2.49 and 2.67 Å observed in the crystal structure of JMJD2A are not observed during XAS analysis.²² These results are consistent with the active site structures of other non-heme iron dioxygenases, which show ligation of the iron center by a 2-His-1-carboxylate facial triad and water molecules.⁷¹ XAS results obtained for resting JMJD2A (with iron in the active site) also show the presence of a four-coordinate zinc site involving one imidazole and three other sulfur donor ligands (Table 3). This is consistent with the Cys₃HisZn site in the crystal structure of the catalytic domain of JMJD2A²² and JMJD2D, and confirms the presence of the expected zinc site in the reconstituted samples used for XAS.

Crystal structures of the JMJD2 proteins in the presence of α KG or its analogue (Table 1) show that the cofactor binds to the metal center in a bidentate manner, forming a five-membered chelate ring. The EXAFS analyses of the samples of Fe(JMJD2A) and Fe(JMJD2C) prepared in the presence of

α KG are also consistent with the bidentate coordination of α KG to the iron center. XAS results obtained for both Fe(JMJD2A) and Fe(JMJD2C) in the presence of α KG show the presence of a five-coordinate iron site involving two imidazole ligands, a bidentate α KG and one other N/O donor ligand, presumably the active site Glu residue (Table 3) observed in the crystal structure of JMJD2A in the presence of α KG.²² The distances obtained for the second-sphere carbon atoms of α KG (2.62 and 2.72 Å for JMJD2A and 2.64 and 2.74 Å for JMJD2C) using XAS are much shorter than those observed in the crystal structure (3.26 and 3.29 Å) of Fe(JMJD2A) in the presence of α KG.²² However, similar M–C distances (obtained using XAS analysis) have been observed in human ABH2 complexed with α KG by XAS,³⁵ the crystal structure of ABH3 complexed with α KG (2.82–2.84 Å),⁷² the crystal structure of human FIH in complex with α KG (2.66–2.88 Å),⁷³ the crystal structure of *Caenorhabditis elegans* lysine specific demethylase 7 A (ceKDM7A) complexed with α KG (2.69–2.73 Å),⁷⁴ the crystal structure of human PHD2 complexed with α KG (2.77–2.87 Å),⁷⁵ and the crystal structure of human JMJD3 complexed with α KG (2.76–2.86 Å).⁷⁶ The shorter distances observed in XAS could be due to the fact that XAS data were collected at 4 K, and therefore, one will expect slightly shorter distances. It is important to note that some of these crystal structures show considerable flexibility of the α KG chelate ring because of the shorter M–C distances compared to those required for symmetrical coordination of a bidentate α KG. In FIH and ceKDM7A, the O–C–C–O five-membered chelate ring undergoes a rotation with respect to the metal ion's equatorial plane (M–O–C–C dihedral angle of $\sim 19^\circ$). On the other hand, in ABH3, JMJD3, and PHD2, the rotation of the five-membered chelate ring with respect to the metal ion's equatorial plane is much smaller (M–O–C–C dihedral angle of $\sim 10^\circ$). Thus, the M–C distances obtained from XAS analysis for JMJD2A and JMJD2C reflect the range of these conformations. In the presence of both α KG and substrate, both JMJD2A and JMJD2C retain the five-coordinate iron site and the second-sphere carbon atoms of α KG are observed at

2.68 and 2.78 Å for Fe(JMJD2A) and 2.73 and 2.83 Å for Fe(JMJD2C). These results are in agreement with the crystal structure of AlkB in complex with Fe(II) in the presence of both α KG and a methylated trinucleotide (2.87–2.93 Å),⁷⁷ the crystal structure of *E. coli* TauD complexed with Fe(II) in the presence of both α KG and a substrate (2.57–2.85 Å),^{78,79} and the crystal structure of FIH complexed with both α KG and a substrate (2.64–2.70 Å).^{80,81}

The results obtained from XAS analysis of the Ni(II)-substituted JMJD2A and JMJD2C are in agreement with the crystal structure of JMJD2D.²⁷ These structures show a six-coordinate nickel site involving two imidazole ligands and four other N/O donor ligands, which are identified in the crystal structure as Glu of the 2-His-1-carboxylate motif and water molecules. The EXAFS analysis of the samples of Ni(JMJD2A) and Ni(JMJD2C) prepared in the presence of α KG indicates the coordination of α KG to the nickel center in a bidentate manner (the second-sphere carbon atoms of α KG are observed at 2.67 and 2.69 Å for JMJD2A and 2.76 and 2.78 Å for JMJD2C). In the presence of α KG, both Ni(JMJD2A) and Ni(JMJD2C) have six-coordinate nickel sites involving two imidazole ligands, a bidentate α KG and two other N/O donor ligands, which are likely active site Glu and a water molecule observed in the crystal structure of Ni(JMJD2C) in the presence of N-OG. These results are in agreement with the crystal structure of Ni(JMJD2A) with N-OG (2.85–2.90 Å),²⁴ the crystal structure of KIAA1718 (a human Jumonji demethylase) with N-OG (2.59–2.62 Å),⁸² and the crystal structure of human PHF2 with N-OG (2.82–2.86 Å).⁸³ In the presence of both α KG and a substrate, both Ni(JMJD2A) and Ni(JMJD2C) retain the six-coordinate nickel site and the second-coordination sphere carbon atoms of α KG are observed at 2.65 and 2.67 Å for Ni(JMJD2A) and 2.63 and 2.65 Å for Ni(JMJD2C). These results are in agreement with the crystal structure of human γ -butyrobetaine 2-oxoglutarate dioxygenase 1 (2.71–2.72 Å, PDB entry 3MSS), the crystal structure of Ni(JMJD2A) with α KG and a substrate (2.81–2.82 Å),²⁵ and the crystal structure of a H3K9 Jumonji demethylase (2.80–2.85 Å).⁸⁴

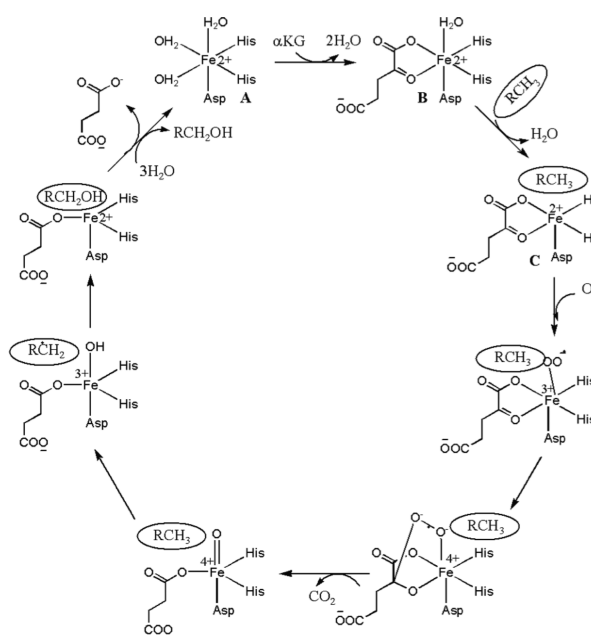
Comparison of XAS Results for DNA and Histone Demethylases. XAS was previously conducted for AlkB⁸⁵ (*E. coli* DNA demethylase) and ABH2³⁵ (human DNA demethylase). Both the DNA demethylases and the histone demethylases are Fe(II)- and α KG-dependent mononuclear non-heme iron enzymes. JMJD2A and JMJD2C have a five-coordinate iron site in the resting state, similar to the results obtained for Fe(AlkB) and Fe(ABH2). The maintenance of a five-coordinate iron site in the binary and ternary complex is observed for ABH2 and JMJD2 proteins. In both cases, the iron K-edge energy decreases from the resting enzyme to the α KG complex, and again to the α KG–substrate complex. This is expected for an iron site that will eventually bind and reductively activate O₂. Remarkably, the iron K-edge energy (7122.5 eV) of the α KG complex is the same for ABH2 and JMJD2 proteins. This is due to the very similar active site (2-His-1-carboxylate and α KG) for ABH2 and JMJD2 proteins. However, the iron K-edge energies for the resting ABH2 and JMJD2 proteins are different [7125.9(2) eV for ABH2 vs 7123.1(2) eV for JMJD2A and 7122.9(2) eV for JMJD2C]. This could be attributed to the ascorbate binding shown for ABH2.³⁵ Also, the iron K-edge energies for the ABH2 and JMJD2 proteins are different [7121.5(2) eV for ABH2 vs 7121.9(2) eV for JMJD2A and 7122.1(2) eV for JMJD2C] in

the presence of the substrate. This could be due to differences in the nature of the substrate (DNA vs histone protein) and also in active site environment for ABH2 and JMJD2 proteins. The Ni complexes of ABH2 are five-coordinate (resting state and in the presence of α KG) and six-coordinate (in the presence of both α KG and a substrate). All of the Ni complexes are six-coordinate for JMJD2 proteins. The Ni K-edge energies for ABH2 do not show any systematic shift, and they are within experimental error for JMJD2 proteins. These results indicate very little change in electron density at the nickel center in the presence or absence of α KG or a substrate for both ABH2 and JMJD2 proteins.

Mechanistic Implications from the XAS Results of Iron-Containing and Nickel-Substituted JMJD2 Proteins.

Characterization of a number non-heme Fe(II) oxygenases has revealed that they function by a sequential reaction mechanism (Scheme 1).^{86–89} In the first step of the consensus mechanism,

Scheme 1. Consensus Mechanism of Non-Heme Fe(II) Dioxygenases^a



^aAdapted from ref 90.

α KG displaces two aqua ligands (Scheme 1, B) from the six-coordinate metal site composed of the 2-His-1-carboxylate facial triad and three aqua ligands (Scheme 1, A). In the next step, an empty coordination site for O₂ binding will open up because of the loss of the remaining aqua ligand in the presence of both α KG and a substrate (Scheme 1, C). Subsequently, oxidative decarboxylation of α KG takes place, leading to the formation of an Fe(IV)=O species.⁹⁰ In the case of the JMJD2 proteins, the Fe(IV)=O species will hydroxylate the methyl group on the N atom of lysine in the histone tail, resulting in the formation of an alcohol, which then forms formaldehyde and a Lys with one fewer methyl group on the N atom in the histone tail (Figure 1).

The XAS studies of the structures of early intermediates (prior to O₂ binding) in the JMJD2A and JMJD2C reaction cycles show that they appear to operate by a variation of the consensus mechanism. XANES and EXAFS analyses are consistent with a five-coordinate Fe(II) site composed of N/

O donor ligands in both JMJD2A and JMJD2C in the resting state (Table 3). Analysis of features from scattering atoms in the second and third coordination spheres indicates that two of these ligands are histidine imidazoles, consistent with the available crystallographic data that show the remaining ligands are presumably derived from Glu and water. The data from the complexes formed with α KG are consistent with the cofactor binding to Fe(II) in a bidentate manner in both JMJD2A and JMJD2C, while retaining the five-coordinate geometries of the complexes (Table 3). Thus, binding of α KG does not change the coordination number of the metal center but perturbs the electronic environment of the metal center by replacing two aqua ligands with anionic O donors. This is similar to the results obtained for Cu- or Fe-Tfda.⁴⁴ Once the substrate has bound, the iron site remains five-coordinate (Table 3) in both JMJD2A and JMJD2C. The formation of a five-coordinate iron site in the presence of both a substrate and α KG has been observed in the consensus mechanism of other α KG-dependent enzymes.^{86–89} However, the iron K-edge energy decreases in the presence of a substrate. This indicates a change in the electronic environment at the metal center in the presence of a substrate. The presence of a five-coordinate iron site in the resting enzyme (Table 3) and its maintenance through ternary complex formation are not unprecedented in DNA or histone demethylases. The crystal structure of JMJD2A in the presence and absence of α KG reveals a five-coordinate iron site.²² The crystal structure of KIAA1718 in the presence of α KG also has a five-coordinate iron site.⁸²

JMJD2A and JMJD2C demethylate the same histone tail Lys residues (H3K9 and K3K36).⁶⁷ This similarity is consistent with their high degree of sequence homology. They are also similar in their methylation state selectivity as they demethylate both dimethylated and trimethylated Lys residues.⁶⁸ It has been suggested that methylation state selectivity will depend on the orientation of the substrate methyl groups toward an Fe(IV)=O intermediate in the enzyme–substrate complex.²⁵ The XAS results presented here show that the resting enzyme, the enzyme– α KG complex, and the enzyme– α KG + substrate complex are similar for both JMJD2A and JMJD2C (Table 3). Thus, these results are consistent with the similar activity of JMJD2A and JMJD2C.

Substitution of iron with other metals in JMJD2 proteins would be expected to yield an enzyme with altered function because of the differences in the ability of the metal site to bind and decarboxylate α KG and/or bind and activate O₂. XANES and EXAFS analyses are consistent with a six-coordinate site composed of N/O donor ligands for nickel in both JMJD2A and JMJD2C in the presence and absence of a cofactor and/or substrate (Table 3). Analysis of features from scattering atoms in the second and third coordination shells indicates that two of these ligands are histidine imidazoles, consistent with the available crystallographic data, and the remaining ligands are presumably derived from Glu and water (and/or α KG).^{24,25}

One possible mechanism of nickel-induced inhibition of JMJD2 proteins would be to use the protein conformation to block the access of O₂ to the iron site as observed in AlkB, the *E. coli* DNA demethylase that catalyzes demethylation of methylated DNA bases.^{91,92} Like human JMJD2 proteins, AlkB is a mononuclear non-heme Fe(II) enzyme that utilizes α KG and O₂ to conduct the oxidative demethylation of its substrate. Both of these enzymes also utilize the 2-His-1-carboxylate motif to bind Fe(II). There are several crystal structures of AlkB reported in the literature in which the Fe(II) in the catalytic

center has been replaced with Mn(II), Co(II), or Ni(II) in presence of both α KG and a substrate.^{77,93–95} All of the metal-substituted AlkB enzymes are catalytically inactive. Comparison of crystal structures of AlkB containing Fe(II), Co(II), or Mn(II) in the presence of both α KG and substrate shows that the positioning of Trp178 and Leu184 is different in the case of Mn(II) or Co(II) than in the case of Fe(II).^{77,95} In the case of Mn(II) and Co(II), Trp178 blocks the O₂ binding site and Leu184 blocks the O₂ diffusion tunnel. The positioning of these residues can also place O₂ in a nonreactive mode (e.g., decreased O₂ binding affinity) in a manner analogous to that of the distal H58Y mutation in hemoglobin.⁸³

There are several possible mechanisms of inhibition of JMJD2 proteins involving Ni(II). Among these possibilities are, first, that Ni(II) in a ligand environment consisting of the 2-His-1-carboxylate motif and an α KG ligand would not be expected to possess a redox potential capable of reductively activating O₂.^{96–98} Consistent with this is the observation that the electron density buildup that occurs on the Fe(II) center upon binding of α KG and then a substrate is not observed for Ni(II). Second, the ternary complex formed among Ni(II)-JMJD2 proteins, α KG, and a substrate contains a six-coordinate nickel site (Table 3) that has no open coordination site for O₂ binding. This six-coordinate Ni(II) complex is indistinguishable from the Ni(II) center in the crystal structure of JMJD2A in the presence of α KG and H3K9Me₃,²⁴ JMJD2C in the presence of N-OG, and the Mn(II) center in the crystal structure of ABH2 in the presence of α KG and dsDNA.⁹³

In summary, using JMJD2A and JMJD2C as examples, we show that members of the JMJD2 family of histone demethylases are inhibited by Ni(II) ions. Using XAS, we show that the inhibition of these enzymes by nickel is due to the presence of nickel in the active site instead of iron. Also, the presence of nickel in the active site does not prevent the binding of the α KG cofactor. This inhibition of JMJD2A and JMJD2C by Ni(II) appears to involve both electronic and steric factors.

■ ASSOCIATED CONTENT

● Supporting Information

Figures of enzyme activity assays of JMJD2A and JMJD2C and tables of EXAFS fits to iron, nickel, and zinc K-edge data used to select the best-fit models. This material is available free of charge via the Internet at <http://pubs.acs.org>.

■ AUTHOR INFORMATION

Corresponding Author

*E-mail: mmaroney@chem.umass.edu. Phone: (413) 545-4876. Fax: (413) 545-4490.

Funding

This work was supported by National Institutes of Health Grant ES005512-P30ES000260 (M.C.).

Notes

The authors declare no competing financial interest.

■ ACKNOWLEDGMENTS

We thank Dr. Yang Shi for providing pGEX-4T-1-GST-JMJD2A and pET28a-His₆-JMJD2C constructs. The Stanford Synchrotron Radiation Laboratory (SSRL) is a national user facility operated by Stanford University on behalf of the U.S. Department of Energy, Office of Basic Energy Sciences. The SSRL Structural and Molecular Biology Program is supported

by the Department of Energy, Office of Biological and Environmental Research, and by the National Institutes of Health, National Center for Research Resources, Biomedical Technology Program.

■ ABBREVIATIONS

JMJD2, Jumonji domain-containing histone demethylase 2; α KG, 2-oxopentanedioic acid; BSA, bovine serum albumin; DNase, deoxyribonuclease; EDTA, ethylenediaminetetraacetic acid; HEPES, 4-(2-hydroxyethyl)-1-piperazineethanesulfonic acid; ICP-OES, inductively coupled plasma-optical emission spectroscopy; N-OG, N-oxalylglycine; PDB, Protein Data Bank; PMSF, phenylmethanesulfonyl fluoride; TCEP, tris(2-carboxyethyl)phosphine; EXAFS, extended X-ray absorption fine structure; XANES, X-ray absorption near-edge structure; XAS, X-ray absorption spectroscopy.

■ REFERENCES

- (1) Doll, R., and Morgan, L. G. (1970) Cancers of Lung and Nasal Sinuses in Nickel Workers. *Br. J. Cancer* 24, 623–632.
- (2) Doll, R., Mathews, J. D., and Morgan, L. G. (1977) Cancers of Lung and Nasal Sinuses in Nickel Workers: Reassessment of Period of Risk. *Br. J. Ind. Med.* 34, 102–105.
- (3) Sunderman, F. W. (1984) Carcinogenicity of Nickel Compounds in Animals. *IARC Sci. Publ.* 53, 127–132.
- (4) Oller, A. R., Costa, M., and Oberdorster, G. (1997) Carcinogenicity assessment of selected nickel compounds. *Toxicol. Appl. Pharmacol.* 143, 152–166.
- (5) Grimsrud, T. K., Berge, S. R., Haldorsen, T., and Andersen, A. (2002) Exposure to different forms of nickel and risk of lung cancer. *Am. J. Epidemiol.* 156, 1123–1132.
- (6) Rojas, E., Herrera, L. A., Poirier, L. A., and Ostrosky-Wegman, P. (1999) Are metals dietary carcinogens? *Mutat. Res., Genet. Toxicol. Environ. Mutagen.* 443, 157–181.
- (7) IARC (1990) *Monograph on the Evaluation of Carcinogenic Risks to Humans. Chromium, Nickel and Welding*, World Health Organization, Lyon, France.
- (8) IARC (2004) *Monographs on the Evaluation of Carcinogenic Risk to Humans. Some Drinking-water Disinfectants and Contaminants, including Arsenic*, World Health Organization, Lyon, France.
- (9) Lee, Y. W., Klein, C. B., Kargacin, B., Salnikow, K., Kitahara, J., Dowjat, K., Zhitkovich, A., Christie, N. T., and Costa, M. (1995) Carcinogenic Nickel Silences Gene-Expression by Chromatin Condensation and DNA Methylation: A New Model for Epigenetic Carcinogens. *Mol. Cell. Biol.* 15, 2547–2557.
- (10) Rossman, T. G. (2003) Mechanism of arsenic carcinogenesis: An integrated approach. *Mutat. Res., Fundam. Mol. Mech. Mutagen.* 533, 37–65.
- (11) Kargacin, B., Klein, C. B., and Costa, M. (1993) Mutagenic Responses of Nickel Oxides and Nickel Sulfides in Chinese-Hamster V79 Cell-Lines at the Xanthine Guanine Phosphoribosyl Transferase Locus. *Mutat. Res.* 300, 63–72.
- (12) Chen, H., and Costa, M. (2009) Iron- and 2-oxoglutarate-dependent dioxygenases: An emerging group of molecular targets for nickel toxicity and carcinogenicity. *BioMetals* 22, 191–196.
- (13) Chen, H. B., Ke, Q. D., Kluz, T., Yan, Y., and Costa, M. (2006) Nickel ions increase histone H3 lysine 9 dimethylation and induce transgene silencing. *Mol. Cell. Biol.* 26, 3728–3737.
- (14) Chen, H. B., Giri, N. C., Zhang, R. H., Yamane, K., Zhang, Y., Maroney, M., and Costa, M. (2010) Nickel Ions Inhibit Histone Demethylase JMJD1A and DNA Repair Enzyme ABH2 by Replacing the Ferrous Iron in the Catalytic Centers. *J. Biol. Chem.* 285, 7374–7383.
- (15) Chervona, Y., Arita, A., and Costa, M. (2012) Carcinogenic metals and the epigenome: Understanding the effect of nickel, arsenic, and chromium. *Metallomics* 4, 619–627.

- (16) Whetstone, J. R., Nottke, A., Lan, F., Huarte, M., Smolnikov, S., Chen, Z. Z., Spooner, E., Li, E., Zhang, G. Y., Colaiacovo, M., and Shi, Y. (2006) Reversal of histone lysine trimethylation by the JMJD2 family of histone demethylases. *Cell* 125, 467–481.
- (17) Ishimura, A., Terashima, M., Kimura, H., Akagi, K., Suzuki, Y., Sugano, S., and Suzuki, T. (2009) Jmjd2c histone demethylase enhances the expression of Mdm2 oncogene. *Biochem. Biophys. Res. Commun.* 389, 366–371.
- (18) Cloos, P. A. C., Christensen, J., Agger, K., and Helin, K. (2008) Erasing the methyl mark: Histone demethylases at the center of cellular differentiation and disease. *Genes Dev.* 22, 1115–1140.
- (19) Gray, S. G., Iglesias, A. H., Lizcano, F., Villanueva, R., Camelo, S., Jingu, H., Teh, B. T., Koibuchi, N., Chin, W. W., Kokkotou, E., and Dangond, F. (2005) Functional characterization of JMJD2A, a histone deacetylase- and retinoblastoma-binding protein. *J. Biol. Chem.* 280, 28507–28518.
- (20) Wissmann, M., Yin, N., Muller, J. M., Greschik, H., Fodor, B. D., Jenuwein, T., Vogler, C., Schneider, R., Gunther, T., Buettner, R., Metzger, E., and Schule, R. (2007) Cooperative demethylation by JMJD2C and LSD1 promotes androgen receptor-dependent gene expression. *Nat. Cell Biol.* 9, 347–353.
- (21) Cloos, P. A. C., Christensen, J., Agger, K., Maiolica, A., Rappasber, J., Antal, T., Hansen, K. H., and Helin, K. (2006) The putative oncogene GASC1 demethylates tri- and dimethylated lysine 9 on histone H3. *Nature* 442, 307–311.
- (22) Chen, Z. Z., Zang, J. Y., Whetstone, J., Hong, X., Davrazou, F., Kutateladze, T. G., Simpson, M., Mao, Q. L., Pan, C. H., Dai, S. D., Hagman, J., Hansen, K., Shi, Y., and Zhang, G. Y. (2006) Structural insights into histone demethylation by JMJD2 family members. *Cell* 125, 691–702.
- (23) Chen, Z. Z., Zang, J. Y., Kappler, J., Hong, X., Crawford, F., Wang, Q., Lan, F., Jiang, C. Y., Whetstone, J., Dai, S., Hansen, K., Shi, Y., and Zhang, G. (2007) Structural basis of the recognition of a methylated histone tail by JMJD2A. *Proc. Natl. Acad. Sci. U.S.A.* 104, 10818–10823.
- (24) Couture, J. F., Collazo, E., Ortiz-Tello, P. A., Brunzelle, J. S., and Trievel, R. C. (2007) Specificity and mechanism of JMJD2A, a trimethyllysine-specific histone demethylase. *Nat. Struct. Mol. Biol.* 14, 689–695.
- (25) Ng, S. S., Kavanagh, K. L., McDonough, M. A., Butler, D., Pilka, E. S., Lienard, B. M. R., Bray, J. E., Savitsky, P., Gileadi, O., von Delft, F., Rose, N. R., Offer, J., Scheinost, J. C., Borowski, T., Sundstrom, M., Schofield, C. J., and Oppermann, U. (2007) Crystal structures of histone demethylase JMJD2A reveal basis for substrate specificity. *Nature* 448, 87–91.
- (26) Chowdhury, R., Yeoh, K. K., Tian, Y. M., Hillringhaus, L., Bagge, E. A., Rose, N. R., Leung, I. K. H., Li, X. S., Woon, E. C. Y., Yang, M., McDonough, M. A., King, O. N., Clifton, I. J., Klose, R. J., Claridge, T. D. W., Ratcliffe, P. J., Schofield, C. J., and Kawamura, A. (2011) The oncometabolite 2-hydroxyglutarate inhibits histone lysine demethylases. *EMBO Rep.* 12, 463–469.
- (27) Krishnan, S., and Trievel, R. C. (2013) Structural and Functional Analysis of JMJD2D Reveals Molecular Basis for Site-Specific Demethylation among JMJD2 Demethylases. *Structure* 21, 98–108.
- (28) Rose, N. R., Woon, E. C. Y., Tumber, A., Walport, L. J., Chowdhury, R., Li, X. S., King, O. N. F., Lejeune, C., Ng, S. S., Krojer, T., Chan, M. C., Rydzik, A. M., Hopkinson, R. J., Che, K. H., Daniel, M., Strain-Damerell, C., Gileadi, C., Kochan, G., Leung, I. K. H., Dunford, J., Yeoh, K. K., Ratcliffe, P. J., Burgess-Brown, N., von Delft, F., Muller, S., Marsden, B., Brennan, P. E., McDonough, M. A., Oppermann, U., Klose, R. J., Schofield, C. J., and Kawamura, A. (2012) Plant Growth Regulator Daminozide Is a Selective Inhibitor of Human KDM2/7 Histone Demethylases. *J. Med. Chem.* 55, 6639–6643.
- (29) Rose, N. R., Woon, E. C. Y., Kingham, G. L., King, O. N. F., Mecinovic, J., Clifton, I. J., Ng, S. S., Talib-Hardy, J., Oppermann, U., McDonough, M. A., and Schofield, C. J. (2010) Selective Inhibitors of the JMJD2 Histone Demethylases: Combined Nondenaturing Mass

Spectrometric Screening and Crystallographic Approaches. *J. Med. Chem.* 53, 1810–1818.

(30) Chang, K.-H., King, O. N. F., Tumber, A., Woon, E. C. Y., Heightman, T. D., McDonough, M. A., Schofield, C. J., and Rose, N. R. (2011) Inhibition of Histone Demethylases by 4-Carboxy-2,2'-Bipyridyl Compounds. *ChemMedChem* 6, 759–764.

(31) King, O. N. F., Li, X. S., Sakurai, M., Kawamura, A., Rose, N. R., Ng, S. S., Quinn, A. M., Rai, G., Mott, B. T., Beswick, P., Klose, R. J., Oppermann, U., Jadhav, A., Heightman, T. D., Maloney, D. J., Schofield, C. J., and Simeonov, A. (2010) Quantitative High-Throughput Screening Identifies 8-Hydroxyquinolines as Cell-Active Histone Demethylase Inhibitors. *PLoS One* 5, e15535.

(32) Woon, E. C. Y., Tumber, A., Kawamura, A., Hillringhaus, L., Ge, W., Rose, N. R., Ma, J. H. Y., Chan, M. C., Walport, L. J., Che, K. H., Ng, S. S., Marsden, B. D., Oppermann, U., McDonough, M. A., and Schofield, C. J. (2012) Linking of 2-Oxoglutarate and Substrate Binding Sites Enables Potent and Highly Selective Inhibition of JmJc Histone Demethylases. *Angew. Chem., Int. Ed.* 51, 1631–1634.

(33) Smith, P. K., Krohn, R. I., Hermanson, G. T., Mallia, A. K., Gartner, F. H., Provenzano, M. D., Fujimoto, E. K., Goeke, N. M., Olson, B. J., and Klenk, D. C. (1985) Measurement of Protein Using Bicinchoninic Acid. *Anal. Biochem.* 150, 76–85.

(34) Higgins, K. A., Hu, H. D. Q., Chivers, P. T., and Maroney, M. J. (2013) Effects of Select Histidine to Cysteine Mutations on Transcriptional Regulation by *Escherichia coli* RcnR. *Biochemistry* 52, 84–97.

(35) Giri, N. C., Sun, H., Chen, H. B., Costa, M., and Maroney, M. J. (2011) X-ray Absorption Spectroscopy Structural investigation of Early Intermediates in the Mechanism of DNA Repair by Human ABH2. *Biochemistry* 50, 5067–5076.

(36) Padden, K. M., Krebs, J. F., MacBeth, C. E., Scarrow, R. C., and Borovik, A. S. (2001) Immobilized metal complexes in porous organic hosts: Development of a material for the selective and reversible binding of nitric oxide. *J. Am. Chem. Soc.* 123, 1072–1079.

(37) Webb, S. M. (2005) SIXpack: A graphical user interface for XAS analysis using IFEFFIT. *Phys. Scr. T115*, 1011–1014.

(38) Ankudinov, A. L., Ravel, B., Rehr, J. J., and Conradson, S. D. (1998) Real-space multiple-scattering calculation and interpretation of X-ray-absorption near-edge structure. *Phys. Rev. B* 58, 7565–7576.

(39) Newville, M. (2001) EXAFS analysis using FEFF and FEFFIT. *J. Synchrotron Radiat.* 8, 96–100.

(40) Zabinsky, S. I., Rehr, J. J., Ankudinov, A., Albers, R. C., and Eller, M. J. (1995) Multiple-Scattering Calculations of X-ray-Absorption Spectra. *Phys. Rev. B* 52, 2995–3009.

(41) Colpas, G. J., Maroney, M. J., Bagyinka, C., Kumar, M., Willis, W. S., Suib, S. L., Baidya, N., and Mascharak, P. K. (1991) X-ray Spectroscopic Studies of Nickel-Complexes, with Application to the Structure of Nickel Sites in Hydrogenases. *Inorg. Chem.* 30, 920–928.

(42) Randall, C. R., Shu, L. J., Chiou, Y. M., Hagen, K. S., Ito, M., Kitajima, N., Lachicotte, R. J., Zang, Y., and Que, L. (1995) X-ray-Absorption Pre-Edge Studies of High-Spin Iron(II) Complexes. *Inorg. Chem.* 34, 1036–1039.

(43) Westre, T. E., Kennepohl, P., DeWitt, J. G., Hedman, B., Hodgson, K. O., and Solomon, E. I. (1997) A multiplet analysis of Fe K-edge 1s → 3d pre-edge features of iron complexes. *J. Am. Chem. Soc.* 119, 6297–6314.

(44) Coper, N. J., Stalhandske, C. M. V., Saari, R. E., Hausinger, R. P., and Scott, R. A. (1999) X-ray absorption spectroscopic analysis of Fe(II) and Cu(II) forms of a herbicide-degrading α -ketoglutarate dioxygenase. *J. Biol. Inorg. Chem.* 4, 122–129.

(45) Costello, A., Periyannan, G., Yang, K. W., Crowder, M. W., and Tierney, D. L. (2006) Site-selective binding of Zn(II) to metallo- β -lactamase L1 from *Stenotrophomonas maltophilia*. *J. Biol. Inorg. Chem.* 11, 351–358.

(46) Costello, A. L., Sharma, N. P., Yang, K. W., Crowder, M. W., and Tierney, D. L. (2006) X-ray absorption spectroscopy of the zinc-binding sites in the class B2 metallo- β -lactamase ImiS from *Aeromonas veronii* bv. *sobria*. *Biochemistry* 45, 13650–13658.

(47) Kim, Y. J., Feng, X. D., and Lippard, S. J. (2007) Synthesis, structure, and properties of a mixed-valent triiron complex of tetramethyl reductic acid, an ascorbic acid analogue, and its relationship to a functional non-heme iron oxidation catalyst system. *Inorg. Chem.* 46, 6099–6107.

(48) Jacquamet, L., Aberdam, D., Adrait, A., Hazemann, J. L., Latour, J. M., and Michaud-Soret, I. (1998) X-ray absorption spectroscopy of a new zinc site in the fur protein from *Escherichia coli*. *Biochemistry* 37, 2564–2571.

(49) Barlow, J. N., Zhang, Z. H., John, P., Baldwin, J. E., and Schofield, C. J. (1997) Inactivation of 1-aminocyclopropane-1-carboxylate oxidase involves oxidative modifications. *Biochemistry* 36, 3563–3569.

(50) Zhang, Z. H., Barlow, J. N., Baldwin, J. E., and Schofield, C. J. (1997) Metal-catalyzed oxidation and mutagenesis studies on the iron(II) binding site of 1-aminocyclopropane-1-carboxylate oxidase. *Biochemistry* 36, 15999–16007.

(51) Garcia, G. A., Tierney, D. L., Chong, S. R., Clark, K., and PennerHahn, J. E. (1996) X-ray absorption spectroscopy of the zinc site in tRNA-guanine transglycosylase from *Escherichia coli*. *Biochemistry* 35, 3133–3139.

(52) Rohde, J. U., Torelli, S., Shan, X. P., Lim, M. H., Klinker, E. J., Kaizer, J., Chen, K., Nam, W. W., and Que, L. (2004) Structural insights into nonheme alkylperoxoiron(III) and oxoiron(IV) intermediates by X-ray absorption spectroscopy. *J. Am. Chem. Soc.* 126, 16750–16761.

(53) Shearer, J., Scarrow, R. C., and Kovacs, J. A. (2002) Synthetic models for the cysteine-ligated non-heme iron enzyme superoxide reductase: Observation and structural characterization by XAS of an Fe-III-OOH intermediate. *J. Am. Chem. Soc.* 124, 11709–11717.

(54) Padden, K. M., Krebs, J. F., Trafford, K. T., Yap, G. P. A., Rheingold, A. H., Borovik, A. S., and Scarrow, R. C. (2001) Probing the structure of immobilized metal sites in porous organic hosts by X-ray absorption spectroscopy. *Chem. Mater.* 13, 4305–4313.

(55) Rohde, J.-U., Stubna, A., Bominaar, E. L., Munck, E., Nam, W., and Que, L., Jr. (2006) Nonheme oxoiron(IV) complexes of tris(2-pyridylmethyl) amine with cis-monoanionic ligands. *Inorg. Chem.* 45, 6435–6445.

(56) Fujimori, D. G., Barr, E. W., Matthews, M. L., Koch, G. M., Yonce, J. R., Walsh, C. T., Bollinger, J. M., Jr., Krebs, C., and Riggs-Gelasco, P. J. (2007) Spectroscopic evidence for a high-spin Br-Fe(IV)-Oxo intermediate in the α -ketoglutarate-dependent halogenase CytC3 from *Streptomyces*. *J. Am. Chem. Soc.* 129, 13408–13409.

(57) Peterson, C. L., and Laniel, M. A. (2004) Histones and histone modifications. *Curr. Biol.* 14, R546–R551.

(58) Margueron, R., Trojer, P., and Reinberg, D. (2005) The key to development: Interpreting the histone code? *Curr. Opin. Genet. Dev.* 15, 163–176.

(59) Zhang, Y., and Reinberg, D. (2001) Transcription regulation by histone methylation: Interplay between different covalent modifications of the core histone tails. *Gene Dev.* 15, 2343–2360.

(60) Kouzarides, T. (2002) Histone methylation in transcriptional control. *Curr. Opin. Genet. Dev.* 12, 198–209.

(61) Lachner, M., and Jenuwein, T. (2002) The many faces of histone lysine methylation. *Curr. Opin. Cell Biol.* 14, 286–298.

(62) Martin, C., and Zhang, Y. (2005) The diverse functions of histone lysine methylation. *Nat. Rev. Mol. Cell Biol.* 6, 838–849.

(63) Byvoet, P., Shepherd, G. R., Noland, B. J., and Hardin, J. M. (1972) Distribution and Turnover of Labeled Methyl Groups in Histone Fractions of Cultured Mammalian-Cells. *Arch. Biochem. Biophys.* 148, 558–567.

(64) Thomas, G., Hempel, K., and Lange, H. W. (1972) Relative Stability of Lysine-Bound Methyl Groups in Arginine-Rich Histones and Their Subfractions of Ehrlich Ascites Tumor-Cells in-Vitro. *Hoppe-Seyler's Z. Physiol. Chem.* 353, 1423–1428.

(65) Shi, Y. J., Lan, F., Matson, C., Mulligan, P., Whetstone, J. R., Cole, P. A., Casero, R. A., and Shi, Y. (2004) Histone demethylation mediated by the nuclear arnine oxidase homolog LSD1. *Cell* 119, 941–953.

- (66) Tsukada, Y., Fang, J., Erdjument-Bromage, H., Warren, M. E., Borchers, C. H., Tempst, P., and Zhang, Y. (2006) Histone demethylation by a family of JmJc domain-containing proteins. *Nature* 439, 811–816.
- (67) Katoh, M., and Katoh, M. (2004) Identification and characterization of JMJD2 family genes in silico. *Int. J. Oncol.* 24, 1623–1628.
- (68) Hillringhaus, L., Yue, W. W., Rose, N. R., Ng, S. S., Gileadi, C., Loenarz, C., Bello, S. H., Bray, J. E., Schofield, C. J., and Oppermann, U. (2011) Structural and Evolutionary Basis for the Dual Substrate Selectivity of Human KDM4 Histone Demethylase Family. *J. Biol. Chem.* 286, 41616–41625.
- (69) Munoz, A., and Costa, M. (2012) Elucidating the mechanisms of nickel compound uptake: A review of particulate and nano-nickel endocytosis and toxicity. *Toxicol. Appl. Pharmacol.* 260, 1–16.
- (70) Bennett, B. G. (1984) Environmental Nickel Pathways to Man. *IARC Sci. Publ.*, 487–495.
- (71) Que, L., and Ho, R. Y. N. (1996) Dioxygen activation by enzymes with mononuclear non-heme iron active sites. *Chem. Rev.* 96, 2607–2624.
- (72) Sundheim, O., Vagbo, C. B., Bjoras, M., Sousa, M. M. L., Talstad, V., Aas, P. A., Drablos, F., Krokan, H. E., Tainer, J. A., and Slupphaug, G. (2006) Human ABH3 structure and key residues for oxidative demethylation to reverse DNA/RNA damage. *EMBO J.* 25, 3389–3397.
- (73) Dann, C. E., Bruick, R. K., and Deisenhofer, J. (2002) Structure of factor-inhibiting hypoxia-inducible factor 1: An asparaginyl hydroxylase involved in the hypoxic response pathway. *Proc. Natl. Acad. Sci. U.S.A.* 99, 15351–15356.
- (74) Xu, W., Yang, H., Liu, Y., Yang, Y., Wang, P., Kim, S. H., Ito, S., Yang, C., Wang, P., Xiao, M. T., Liu, L. X., Jiang, W. Q., Liu, J., Zhang, J. Y., Wang, B., Frye, S., Zhang, Y., Xu, Y. H., Lei, Q. Y., Guan, K. L., Zhao, S. M., and Xiong, Y. (2011) Oncometabolite 2-Hydroxyglutarate Is a Competitive Inhibitor of α -Ketoglutarate-Dependent Dioxygenases. *Cancer Cell* 19, 17–30.
- (75) Rosen, M. D., Venkatesan, H., Peltier, H. M., Bembenek, S. D., Kanelakis, K. C., Zhao, L. X., Leonard, B. E., Hocutt, F. M., Wu, X. D., Palomino, H. L., Brondstetter, T. I., Haugh, P. V., Cagnon, L., Yan, W., Liotta, L. A., Young, A., Mirzadegan, T., Shankley, N. P., Barrett, T. D., and Rabinowitz, M. H. (2010) Benzimidazole-2-pyrazole HIF Prolyl 4-Hydroxylase Inhibitors as Oral Erythropoietin Secretagogues. *ACS Med. Chem. Lett.* 1, 526–529.
- (76) Kruidenier, L., Chung, C. W., Cheng, Z. J., Liddle, J., Che, K. H., Joberty, G., Bantscheff, M., Bountra, C., Bridges, A., Diallo, H., Eberhard, D., Hutchinson, S., Jones, E., Katso, R., Leveridge, M., Mander, P. K., Mosley, J., Ramirez-Molina, C., Rowland, P., Schofield, C. J., Sheppard, R. J., Smith, J. E., Swales, C., Tanner, R., Thomas, P., Tumber, A., Drewes, G., Oppermann, U., Patel, D. J., Lee, K., and Wilson, D. M. (2012) A selective jumonji H3K27 demethylase inhibitor modulates the proinflammatory macrophage response. *Nature* 488, 404–408.
- (77) Yu, B., and Hunt, J. F. (2009) Enzymological and structural studies of the mechanism of promiscuous substrate recognition by the oxidative DNA repair enzyme AlkB. *Proc. Natl. Acad. Sci. U.S.A.* 106, 14315–14320.
- (78) O'Brien, J. R., Schuller, D. J., Yang, V. S., Dillard, B. D., and Lanzilotta, W. N. (2003) Substrate-induced conformational changes in *Escherichia coli* taurine/ α -ketoglutarate dioxygenase and insight into the oligomeric structure. *Biochemistry* 42, 5547–5554.
- (79) Elkins, J. M., Ryle, M. J., Clifton, I. J., Hotopp, J. C. D., Lloyd, J. S., Burzlaff, N. I., Baldwin, J. E., Hausinger, R. P., and Roach, P. L. (2002) X-ray crystal structure of *Escherichia coli* taurine/ α -ketoglutarate dioxygenase complexed to ferrous iron and substrates. *Biochemistry* 41, 5185–5192.
- (80) Yang, M., Chowdhury, R., Ge, W., Hamed, R. B., McDonough, M. A., Claridge, T. D. W., Kessler, B. M., Cockman, M. E., Ratcliffe, P. J., and Schofield, C. J. (2011) Factor-inhibiting hypoxia-inducible factor (FIH) catalyses the post-translational hydroxylation of histidinyl residues within ankyrin repeat domains. *FEBS J.* 278, 1086–1097.
- (81) Coleman, M. L., McDonough, M. A., Hewitson, K. S., Coles, C., Mecinovic, J., Edelmann, M., Cook, K. M., Cockman, M. E., Lancaster, D. E., Kessler, B. M., Oldham, N. J., Ratcliffe, P. J., and Schofield, C. J. (2007) Asparaginyl hydroxylation of the notch ankyrin repeat domain by factor inhibiting hypoxia-inducible factor. *J. Biol. Chem.* 282, 24027–24038.
- (82) Horton, J. R., Upadhyay, A. K., Qi, H. H., Zhang, X., Shi, Y., and Cheng, X. D. (2010) Enzymatic and structural insights for substrate specificity of a family of jumonji histone lysine demethylases. *Nat. Struct. Mol. Biol.* 17, 38–43.
- (83) Horton, J. R., Upadhyay, A. K., Hashimoto, H., Zhang, X., and Cheng, X. D. (2011) Structural Basis for Human PHF2 Jumonji Domain Interaction with Metal Ions. *J. Mol. Biol.* 406, 1–8.
- (84) Upadhyay, A. K., Rotili, D., Han, J. W., Hu, R. G., Chang, Y. Q., Labella, D., Zhang, X., Yoon, Y. S., Mai, A., and Cheng, X. D. (2012) An Analog of BIX-01294 Selectively Inhibits a Family of Histone H3 Lysine 9 Jumonji Demethylases. *J. Mol. Biol.* 416, 319–327.
- (85) Mishina, Y., Chen, L. X., and He, C. (2004) Preparation and characterization of the native iron(II)-containing DNA repair AlkB protein directly from *Escherichia coli*. *J. Am. Chem. Soc.* 126, 16930–16936.
- (86) Hausinger, R. P. (2004) Fe(II)/ α -ketoglutarate-dependent hydroxylases and related enzymes. *Crit. Rev. Biochem. Mol. Biol.* 39, 21–68.
- (87) Costas, M., Mehn, M. P., Jensen, M. P., and Que, L. (2004) Dioxygen activation at mononuclear nonheme iron active sites: Enzymes, models, and intermediates. *Chem. Rev.* 104, 939–986.
- (88) Hanauskeabel, H. M., and Gunzler, V. A. (1982) Stereochemical Concept for the Catalytic Mechanism of Prolylhydroxylase: Applicability to Classification and Design of Inhibitors. *J. Theor. Biol.* 94, 421–455.
- (89) Solomon, E. I., Brunold, T. C., Davis, M. I., Kemsley, J. N., Lee, S. K., Lehnert, N., Neese, F., Skulan, A. J., Yang, Y. S., and Zhou, J. (2000) Geometric and electronic structure/function correlations in non-heme iron enzymes. *Chem. Rev.* 100, 235–349.
- (90) Bollinger, J. M., Price, J. C., Hoffart, L. M., Barr, E. W., and Krebs, C. (2005) Mechanism of taurine: α -Ketoglutarate dioxygenase (TauD) from *Escherichia coli*. *Eur. J. Inorg. Chem.* 21, 4245–4254.
- (91) Treweek, S. C., Henshaw, T. F., Hausinger, R. P., Lindahl, T., and Sedgwick, B. (2002) Oxidative demethylation by *Escherichia coli* AlkB directly reverts DNA base damage. *Nature* 419, 174–178.
- (92) Falnes, P. O., Johansen, R. F., and Seeberg, E. (2002) AlkB-mediated oxidative demethylation reverses DNA damage in *Escherichia coli*. *Nature* 419, 178–182.
- (93) Yang, C. G., Yi, C. Q., Duguid, E. M., Sullivan, C. T., Jian, X., Rice, P. A., and He, C. (2008) Crystal structures of DNA/RNA repair enzymes AlkB and ABH2 bound to dsDNA. *Nature* 452, 961–965.
- (94) Yu, B., Edstrom, W. C., Benach, J., Hamuro, Y., Weber, P. C., Gibney, B. R., and Hunt, J. F. (2006) Crystal structures of catalytic complexes of the oxidative DNA/RNA repair enzyme AlkB. *Nature* 439, 879–884.
- (95) Holland, P. J., and Hollis, T. (2010) Structural and Mutational Analysis of *Escherichia coli* AlkB Provides Insight into Substrate Specificity and DNA Damage Searching. *PLoS One* 5, e8680.
- (96) Mirza, S. A., Day, R. O., and Maroney, M. J. (1996) Oxidation of a dimeric nickel thiolate complex with O₂. *Inorg. Chem.* 35, 1992–1995.
- (97) Grapperhaus, C. A., and Darensbourg, M. Y. (1998) Oxygen capture by sulfur in nickel thiolates. *Acc. Chem. Res.* 31, 451–459.
- (98) Goldcamp, M. J., Robison, S. E., Bauer, J. A. K., and Baldwin, M. J. (2002) Oxygen reactivity of a nickel(II)-polyoximate complex. *Inorg. Chem.* 41, 2307–2309.